

Numerical Analyses of Optical Fiber Probing for Industrial Bubbly Flows

メタデータ	言語: en 出版者: Shizuoka University 公開日: 2013-11-08 キーワード (Ja): キーワード (En): 作成者: Sakamoto, Akihiro メールアドレス: 所属:
URL	https://doi.org/10.14945/00007459

静岡大学 博士論文

Numerical Analyses of Optical Fiber Probing for Industrial Bubbly Flows

工業規模の気泡流動状態を計測する
光ファイバースプロブの数値解析

2012 年 6 月

大学院 自然科学系教育部

環境・エネルギーシステム専攻

坂本 明洋

Doctoral Thesis

Numerical Analyses of Optical Fiber Probing for Industrial Bubbly Flows

Akihiro Sakamoto

Student ID number: 55945024

Graduate School of Science and Technology, Educational Division,
Department of Environment and Energy Systems,
Shizuoka University

Contents

1. Introduction	1
1.1. Background and objectives of this thesis	
1.2. Numerical analysis of probing signals	
1.3. Algorithm to detect the phase levels	
1.4. Bubble flow measurement	
2. Numerical analysis of the probing signal	8
2.1. Mathematics of ray tracing method	
2.2. Measurement principle of S-TOP	
2.3. Numerical model of optical fiber probing	
2.4. Program framework	
2.5. Experimental setups to verify the numerical model and analyze peak signals	
2.6. Results and discussions	
2.7. Conclusion	
3. Automatic detection of phase signal levels from raw probing signal	41
3.1. Problems of conventional algorithm	
3.2. Algorithms to precisely and rationally detect phase signal levels	
3.3. Experimental results and discussions	

4. Industrial bubble flow measurement	59
4.1. Measurement principle of F-TOP	
4.2. Algorithm to detect bubbles' velocity, diameter and void fraction	
4.3. Categorization of signal noise in industrial sites	
4.4. Large-scale bubble column setup	
4.5. Results and discussions	
4.6. Conclusion	
 5. Conclusion	 82
 Nomenclature	 84
References	85

1. Introduction

1.1. Background and objectives of this thesis

Gas-liquid two-phase flows with a dense dispersed phase are frequently encountered in a wide range of industrial fields: e.g. energy plants, chemical reactors, hot metal cooling processes and automotive fuel injections. Improving their performances is essential for mitigating a discharge amount of green-house gases. For the purpose of experimentally revealing the flows, many measurement techniques have been developing, such as laser-based measurement techniques¹⁸ (e.g. phase Doppler anemometer), visualization techniques³⁷, electric conductivity probes⁶⁻⁸ and optical fiber probes^{1,4,9-13,19-21,23,26,27,29,31,33-41,46-48}. I focused on the optical fiber probes that are intrusive techniques but very reliable and effectual even for the measurement in the industrial plants, in which the nonintrusive measurement techniques are difficult to employ.

Several types of optical fiber probe for simultaneous measurement of diameter, velocity and number density (void fraction or liquid holdup) of bubbles/droplets have been developed and their measurement performance was investigated. Abuaf et al. investigated an optical fiber probe with a controlled tip geometry for unsteady local void fraction and interface velocity measurement in liquid-vapor two-phase flows at the minimum influence of the probe presence to the flows¹. Frijlink investigated several types of axial symmetric optical fiber probes and round-shaped conical probes were most successful¹⁷. In addition, he proposed a basic structure of four-tip fiber arrangement. Cartellier and Barrau researched monofiber optical probes, particularly “conical” probes^{10,11}.

All these researches succeeded in progressing the measurement technology of the gas-liquid two-phase flows and basically their signal analyzing algorithms were limited to abstracting the information of water level, air level and the phase transition times, refining the probing signal to enough binary waveform. The approach is essential but

had two weaknesses: (1) it neglects several peak signals as unavailable noise (2) it was not robust for industrial use in which the probing signal often includes high peak signals.

I investigated carefully whether the high peak signals were removable or not. After removing electrical noise and optical noise, I however found some peak signals still remained and they have a great potential for advanced measurement. For example, our research group found that a wedge-shaped-tip probe often brings out a "pre-signal" that intensively appears only when the probe touches the center region of a bubble frontal interface. The pre-signal is therefore considered very useful to distinguish the touch position on the bubble interface. Indeed, the appearance of the pre-signal has been reported on various optical probing¹⁰⁻¹² and the generating mechanism of the signal has been identified as the reflected lights from the air-water interface. However, the identification does not explain why any pre-signals do not appear when the probe touches the non-center region of a bubble. I therefore developed a numerical simulator to reveal the mechanism for the purpose of positive application of the pre-signal.

To conclude, the first objective of this thesis is to reveal the mechanism of the high peak signals in the probing signals. The second objective of this thesis is to develop a robust algorithm for detecting bubble dynamics from raw probing signals even including the peak signals. The third objective is to confirm the measurement accuracy of the probing in an industrial-scale bubble column.

To solve the first objective, I developed a numerical probing signal simulator based on ray tracing method⁴⁰. The details are described in the section 1.2 and the chapter 2. To solve the second objective, I developed two robust algorithms to detect air and water phase levels, based on histogram analysis³⁹. The details are described in the section 1.3 and the chapter 3. To achieve the third objective, I applied a four-tip optical fiber probe (F-TOP) to measure the bubble's velocity, diameter and void fraction in an industrial-scale bubble column³⁹. The details are described in the section 1.4 and the

chapter 4.

1.2. Numerical analysis of probing signals

To simulate optical phenomena, several numerical models have been proposed. The most fundamental numerical model is based on the Maxwell equation to solve the continuous light wave propagation. For example, Nakamura et al. numerically simulated optical properties of beam propagation in a tapered fiber probe tip of which diameter was around $1\text{ }\mu\text{m}$ and tip diameter was $0.2\text{ }\mu\text{m}$ ^{30,31}. The applied finite-difference time-domain (FDTD) method is a promising technique, however, its computational cost will become high if it is applied on an optical system of mm-order in diameter and m-order in length. Most simulators for optics are therefore based on ray tracing algorithm which traces ray segment trajectories geometrically and is easy to render complex optical boundary conditions.

Ray tracing simulation in early stages was studied for the particular purpose of controlling aberration in designing axisymmetric lens systems. These numerical models based on ABCD (or Smith) matrices technique were employed for reducing the calculation cost. For example, Moore investigated carefully the ray paths in several GRIN (Gradient-index) fibers²⁸. Sweat designed a planar holographic lens by computing the third-order aberrations⁴⁴. The techniques are enough practical for the conventional issues but are not effectual in nonaxisymmetric optical phenomena, for example, wedge-shaped tip probing.

To simulate nonaxisymmetric optical phenomena, a lot of numerical models have been proposed particularly in engineering illumination or in drawing 3D computer graphics. For example, Nicodemus et al. proposed a simple but satisfying quantifiable numerical reflection model called as BRDF (Bidirectional Reflection Distribution Function) model to simulate diffused reflection on walls³². Schlick enhanced the BRDF model introducing approximated Fresnel equations⁴². These techniques provided

enough amount of ray information to photographic images by tracing all ray trajectories, however Fresnel's law was neglected or approximated in their ray objects. By contrast, in numerically analyzing the optical fiber probing, the strict application of the law is required in order to evaluate the energy distribution of reflection and refraction. In addition, some of the techniques employed only flat polygon surface model which was not able to render the exact surfaces of a cylindrical optical fiber and ellipsoidal bubble, and some needed much longer calculation time for a fine computational mesh. These previous techniques are therefore not enough to simulate the output signals of the optical probing.

I developed a new ray-tracing simulator in which each ray object had its own polarization angle and in which the objects surfaces were rendered into free forms³⁹; e.g. cylinders and ellipsoids. The simulator quantifies the probing signals more accurately by tracing the inlet beams, reflected and refracted beams on the objects' surfaces (optical fiber, sensing tip, air interface, water interface, bubble or droplet), and the returned beams passing through the fiber from the sensing tip to the other tip.

As the result, (a) I revealed an optical fiber probe with a wedge-shaped tip has particular characteristics of the beam emissions from the tip and the emitting angles switched depending on the phases covering the tip. This phenomenon is very effective for further advanced optical probing. (b) I derived the cutting angle of the sensing tip maximizing the air signal level was around 30° numerically, therefore this angle is the best for gaining a high S/N ratio in bubble/droplet measurement. (c) I found out the meniscus shape obviously affected on the probing signal optically. (d) I revealed a new mechanism of a pre-signal caused by the reflection at the frontal and rear surface of a bubble. The pre-signal is very useful for practical measurement of a bubble because it appears only when the probe penetrates the center region of the bubble.

I compared and verified the above numerical results with the following experiments of (1) - (3), and obtained the satisfactory correspondence between them. (1) The beam

trajectories and energy leaking out from the sensing tip into the surrounding air phase or water phase. (2) The probing signals throughout penetration of the sensing tip at the air-water free surface in consideration of the three-dimensional surface deformation. (3) The probing signals throughout penetration of the sensing tip into a bubble in consideration of the three-dimensional bubble shape.

1.3. Algorithm to detect the phase levels

In industrial use of optical fiber probes, the probe signals inevitably include many types of noise. Although the phase detection process is essential in optical probing, sometimes the signals corresponding to the gas/liquid phases are buried in noise, and the misdetection of the phases results in decreased measurement accuracy. In order to correctly detect the gas/liquid phase signals from the noisy raw signals, a robust algorithm is needed as an alternative to the conventional algorithm. Furthermore, some signals judged as noise include very useful but latent information. For instance, a signal which sharply appears just before the optical fiber probe touches a frontal surface of a bubble indicates the position pierced by the probe³⁷. In order to detect such meaningful sub-signals, a more sensitive algorithm is needed.

First, I investigated the relations between the noise signal patterns and the noise generation mechanism. Based on the results, I categorized the noise. The noise obtained in the optical fiber probing is grouped into two major categories: noise due to optical phenomena and noise due to electrical phenomena. The optical noise arises from light scattering on the deformed gas-liquid interface when the probe approaches the bubble. Identifying the causes of the optical noise in the industrial setting is very difficult or impossible. The electrical noise arises from the transient responses of electrical units and the power supply. The causes of electrical noises are identifiable and easily removed from the raw signals. Firstly, I carefully investigated the optical noise and its causes, and categorized it into several types.

Second, based on the results, I developed two types of algorithms (Histogram method and Median method), which robustly distinguish the gas and liquid signals from raw signals even containing strong pre-signals and overshoots. Third, I verified the performance of the new algorithms compared with the conventional algorithm of the min-max method on the noisy signals of a single-tip optical-fiber probe (S-TOP). The min-max method was not able to obtain proper parameters to process the noisy signals; however, the new algorithms easily obtained these parameters. Next, a four-tip optical fiber probe (F-TOP) was installed in a large, highly-concentrated and multi-dispersed bubbly column. I demonstrated the algorithms' performance in analyzing the noisy signals obtained from experiments of industrial-scale and industrial-condition bubbly flows. The new algorithms showed definite robustness, and the bubble diameters and velocities obtained by the new processing showed satisfactory agreement with the results obtained by other measurements: namely, a high-speed visualization to measure bubble diameters and velocities and a differential pressure method to measure the void fraction.

1.4. Bubble flow measurement

In order to investigate the performance of the optical fiber probing in industrial use, I carried an experiment to industrial-scale and industrial-condition bubbly flows.

Most previous researches were conducted under laboratory conditions: a small bubble column, a low bubble concentration and mono-dispersed bubbles. For example, Barrau et al. developed real-time signal processing and evaluated their sensor performance via experiments in a narrow bubble column (50 mm in diameter and 5 m in height)⁵. Mudde and Saito researched the hydrodynamic similarities of bubbly flows in a pipe 149 mm in inner diameter and 8 m in height, via four-tip optical fiber probes 0.2 mm in outer diameter and 0.5 mm in radial distance²⁹. Aprin et al. investigated local void fractions of gas–liquid two-phase flows in a tube 15.7 mm in inner diameter and 500 mm in height using a cone-shaped single-tip optical fiber probe with a diameter of 500 μm at the base and 0.4 μm at the tip³. Mahvash and Ross discussed flow patterns in a small pipe 19 mm in inner diameter and 2 m height by using a single-tip optical fiber probe²⁵.

The optical signals of these researches were clear and high quality. In the industrial use of optical fiber probes, such conditions are rare and the probe signals inevitably include many types of noise. I applied the new algorithm to measure a large-scale (260 mm in inner diameter of the column and 6 m in the height) and condensed (5-15% in the void fraction) bubbly flow. The algorithm showed definite robustness, and the bubble diameters and velocities obtained by the new processing showed satisfactory agreement with the results obtained by other measurements: namely, a high-speed visualization to measure bubble diameters and velocities and a differential pressure method to measure the void fraction.

2. Numerical analysis of the probing signal

2.1. Mathematics of ray tracing method

Ray tracing method is well known and useful algorithm but simplifies optical phenomena under some approximations. This section outlines the mathematics of the ray tracing method.

The most primary equation of light propagation is the Maxwell equation:

$$\nabla \times \mathbf{E} = -\frac{\partial}{\partial t} \mathbf{B} \quad , \quad (1)$$

where \mathbf{E} is the electric field and \mathbf{B} is the magnetic field.

The equation has a lot of nonlinear parameters and is very difficult to solve a complex optical setup. Some simplifications are therefore needed for analyzing the optical fiber probing.

Neglecting magnetization, the classical wave equation is derived as:

$$\nabla^2 \mathbf{E} = \left(\frac{n}{c}\right)^2 \frac{\partial^2}{\partial t^2} \mathbf{E} \quad , \quad (2)$$

where n is the refractive index and c is the light velocity.

Supposing n is enough homogeneous in the analysis medium and the light transmits in a lossless medium, the equation (2) is simplified into the following eikonal equation;

$$|\nabla \varphi(\mathbf{r})|^2 = n^2(\mathbf{r}) \quad , \quad (3)$$

where $\varphi(\mathbf{r})$ is the eikonal function and \mathbf{r} is the ray trajectory.

Equation (3) is strictly correct when the wavelength of the light is enough shorter than the sizes of the optical setup. Transforming the unknown eikonal function $\varphi(\mathbf{r})$, the ray equation is derived as follows:

$$\frac{d}{ds}n(\mathbf{r})\frac{d\mathbf{r}}{ds} = \nabla n(\mathbf{r}) , \quad (4)$$

where s is the length between the root point and \mathbf{r} .

In homogeneous media, i.e. $\nabla n(\mathbf{r}) = 0$, the ray transmits straightly and the light wave can be simulated by a number of ray segments geometrically. This is the principle of ray tracing algorithm.

To conclude, the ray tracing method is applicable to conditions of non-magnetized objects, homogeneous and lossless waveguide media, and optics sizes enough larger than the light wavelength. The target optical setup of single-tip optical fiber probing meets to these conditions; i.e. there are no magnetized objects, the step-index optical fiber is enough homogeneous and lossless, and the probe diameter (230 μm) is enough larger than the source light wavelength (500 - 650 nm).

The refractive index n needs to change discontinuously on the interfaces of the water phase, the air phase, and the core and clad of the optical fiber. To simulate the probing signal, the angles and the energy of refraction and reflection have to be quantified on the interfaces. The reflection angle and the refraction angle are implemented by the following equations;

The reflection angle is the same as the incoming angle,

The refraction angle is given by

$$\frac{\sin \theta_t}{\sin \theta_i} = \frac{n_i}{n_t} \quad (\text{Snell's law}), \quad (5)$$

where θ_i , θ_t , n_i , n_t are the incoming angle, the refracting angle, the refractive index of the incoming media and the refractive index of the transmitting media, respectively. If the incoming angle θ_i was bigger than the critical angle $\theta_c (= \sin^{-1}(n_t / n_i))$ when $n_t < n_i$, the refracting angle θ_t has imaginary component and no refracting RAY is generated. This is called as a total reflection in general.

If the refracting angle θ_t had only one real component, the developed simulator

calculates the energy of reflectivity and transmissivity by the following equations derived from Fresnel's equation, assuming the interfaces are enough smooth to neglect random reflection.

Reflectivity:

$$R_p = \frac{\tan^2(\theta_i - \theta_t)}{\tan^2(\theta_i + \theta_t)}, \quad (6)$$

$$R_s = \frac{\sin^2(\theta_i - \theta_t)}{\sin^2(\theta_i + \theta_t)}, \quad (7)$$

where R_p and R_s are reflectivities of parallel and perpendicular (senkrecht) polarization respectively.

Transmissivity:

$$T_p = \frac{\sin(2\theta_i)\sin(2\theta_t)}{\sin^2(\theta_i + \theta_t)\cos^2(\theta_i - \theta_t)}, \quad (8)$$

$$T_s = \frac{\sin(2\theta_i)\sin(2\theta_t)}{\sin^2(\theta_i + \theta_t)}, \quad (9)$$

where T_p and T_s are transmissivities of parallel and perpendicular (senkrecht) polarization, respectively.

2.2. Measurement principle of S-TOP

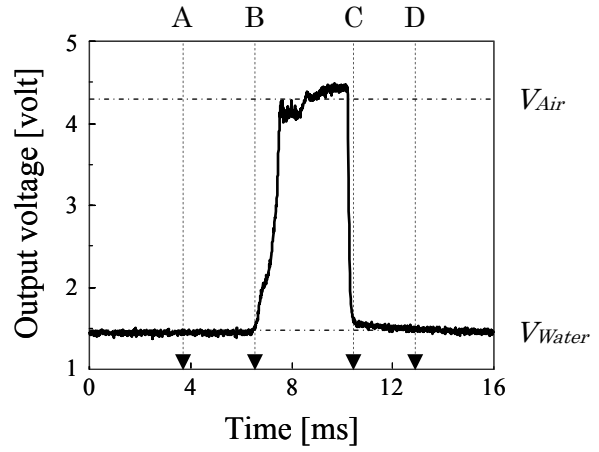
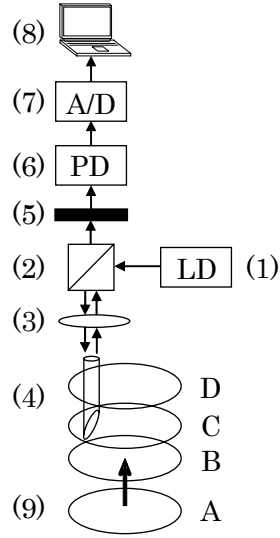
I focused on a wedge-shaped single-tip optical fiber probing (S-TOP) as the object of the numerical analysis, because it was a suitable setup for analyzing the optical phenomena but output suggestive and hopeful signals in the previous experiments³⁷.

Figure 1 describes an optical setup of the S-TOP and a typical signal during the probe piercing a bubble. The probing system consisted of optics (an optical fiber probe, a laser diode, a beam splitter, a polarizer and an objective lens), and a photo-detection system (a photomultiplier, an A/D convertor and a PC). The fiber was a step index type of quartz fiber. The sensing tip was carefully and smoothly ground into a wedge shape

with an angle of around 35 degrees in which the gap of the returned-light intensity between the air phase and water phase became experimentally maximal. The laser beams from the LD made a right-angle turn through the beam splitter. The laser beams focused through the objective lens entered the optical fiber at the inlet tip. The returned beams from the sensing tip went through the beam splitter and polarizer and were detected by the photomultiplier. The output of the photomultiplier was digitized via the A/D convertor and stored into the PC.

The phases are detected based on the intensity differences of the returned beams at the sensing tip in accordance with Snell's law. While the sensing tip is positioned in the water (or liquid in general) phase (the interval of A–B in figure 1), a large part of the incident beams is emitted into the water phase, and the intensity of the returned beams results in being low (water-phase output level V_{Water}). When the sensing tip penetrates the bubble frontal surface B, the signal rapidly increases due to a rapid increase in the returned beam intensity. While the sensing tip is positioned in the air (or gas in general) phase, the signal level is kept high (air-phase output level V_{Air}). Finally, when the sensing tip penetrates the bubble rear surface C, the signal level rapidly decreases, because the sensing tip rapidly changes its position from the air phase to the water phase.

This signal provides the time t_s of the sensing-tip contact with the bubble frontal surface and the time t_e of the sensing-tip penetration of the bubble rear surface. In addition, the gradient of the rising signal B-C is proportional to the vertical velocity component of the bubble frontal surface³⁷. The velocity is nearly equal to the bubble velocity. The bubble velocity v_b is therefore measured from the rising angle, calibrating the proportion of them. In addition, the pierced chord length d_b is obtained from the multiplication of the v_b and the $(t_e - t_s)$. The d_b is equal to the minor axis of the bubble if the probe penetrated the center of the bubble vertically.



(a) Outline of the S-TOP set up

(b) A sample clear signal of the S-TOP

(1) Light source (Laser diode), (2) Beam splitter, (3) Objective lens, (4) S-TOP, (5) Polarizer, (6) Light detector (Photo diode), (7) A/D converter, (8) PC, (9) Bubble.

FIG. 1: Outline of the S-TOP setup and a sample clear signal of the probing.

2.3. Numerical model of optical fiber probing

I developed a numerical simulator for analyzing the S-TOP characteristics based on ray tracing algorithm described in the previous section. Figure 2 outlines the numerical optics of the S-TOP system. The numerical model renders one step-index optical fiber, one bubble and an enormous number of ray segments in a cylindrical space. Each ray has to be traced its rooter, direction, the closest intersection coordinate on a surface, the angle with the surface and the energy ratio of reflection and transmission. This is more complex than past ray tracing studies; i.e., lens system designing software basically can not treat non-axisymmetric optical objects and 3D-CG drawing software neglect or approximate reflectivity or transmissivity. In addition, these systems treat up to two independent-refractive-index optical objects but there are at least four independent-refractive-index objects in the control space.

I therefore developed the numerical simulator based on a 3D-CG ray tracing mathematics¹⁵ adding rigorous reflection and transmission model based on Fresnel's equations. This framework provides more rigorous total simulation of the S-TOP optical phenomena.

The objects are categorized and rendered into three primitive object types: BODY, SURFACE and RAY. Each object has information corresponding to the optical phenomena of S-TOP system and needed for the ray tracing calculation; i.e., a BODY has its homogeneous refractive index, a SURFACE has its 3D shape information and a RAY has its root point and the direction. Several types of SURFACE shape are available for rendering optics; i.e. cut cylinders, ellipses, midair ellipses, ellipsoid, triangle and square. This "free shape" feature is very important in order to improve the accuracy of the numerical simulation and to reduce the computation time.

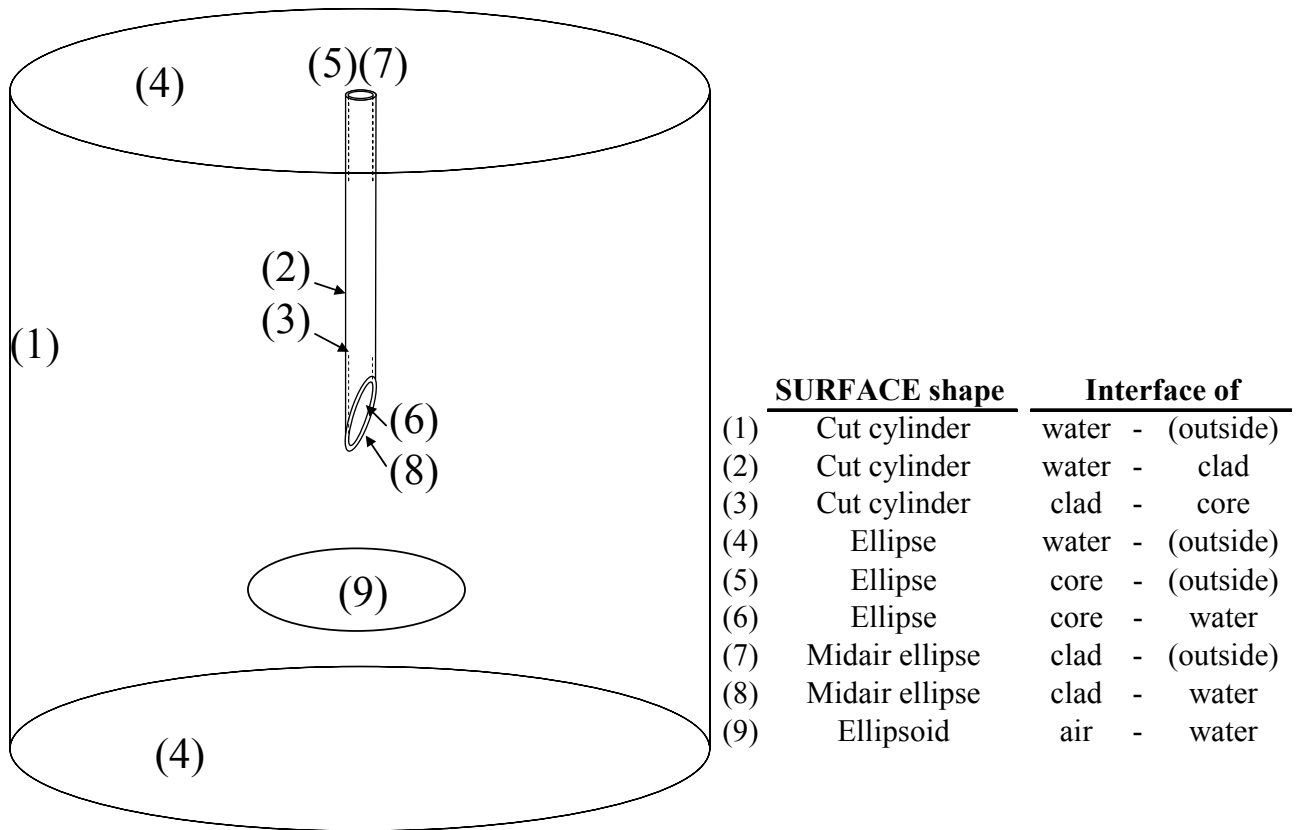


FIG. 2: The numerical SURFACE model of a single-tip optical fiber probing.

As discussing on the section 2.6, I found the meniscus shape greatly affects on the probing signals. Considering this, I implemented an approximated meniscus SURFACE model. Clanet and Quere precisely obtained both of static and dynamic meniscus models around a fine fiber of 0.450 mm in outer diameter¹⁴. The simulation target of the S-TOP has a complex asymmetric tip and it is so complex to obtain the meniscus profile. Further, full coupling of the fluid dynamical issue and the optical issue is not the primary purpose of the present investigation. I therefore approximated the meniscus profile as an axial symmetrically rounded surface with a constant radius. Figure 3 describes the present meniscus model characterized by four parameters of R_l , R_2 , R_m and z_m . Such axial symmetric profile yields a partial overlap with the sensing tip. I minimized the overlap area with fitting the R_2 circle and the R_m meniscus on the sensing tip. The parameters R_l , R_2 and z_m are derived as listed in table 1, depending on a situation of the sensing tip (1) - (4).

The meniscus radius R_m changes in association with the surface tension of the air-water interface, the pressure and the temperature of air and water, the geometry profile of the sensing tip, the wettability and the relative velocity of the interface and the tip. In general the measurement of R_m through experiments was very difficult; hence I assumed the R_m -range from 0.0 mm (flat surface) to 0.4 mm.

In addition, to improve the simulation accuracy, I implemented a bubble SURFACE model of a combination of a couple of half ellipsoids. Figure 4 shows the modeled bubble shape. I changed the ratio of the radii R_{b1} and R_{b2} but kept the minor axis d_b ($= R_{b1} + R_{b2}$) constant based on the results obtained through visualization experiments¹⁶. Further I kept the bubble volume constant.

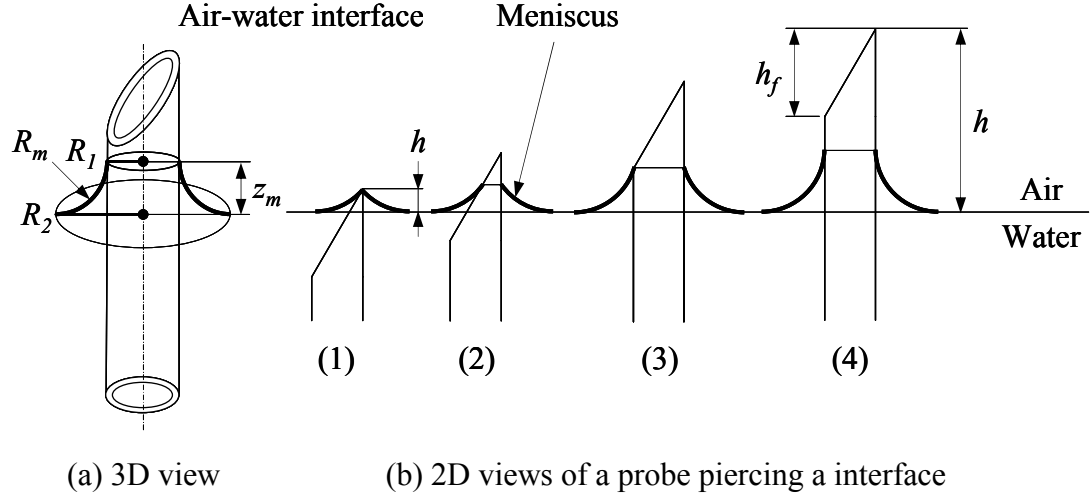


FIG. 3: Meniscus model characterized by four parameters of R_1 , R_2 , R_m and z_m .

Table 1: Parameters for the meniscus model

Situation of sensing tip	R_1	R_2	z_m
(1)	$\sqrt{2R_m h - h^2}$	0	h
(2)	$R_2 + R_m \cos \theta$	$(h - z_m)/(2 \tan \theta)$	$R_m (1 - \sin \theta)$
(3)	$R_{Clad} + \sqrt{2R_m z_m - z_m^2}$	R_{Clad}	$h - h_f$
(4)	$R_{Clad} + R_m$	R_{Clad}	R_m

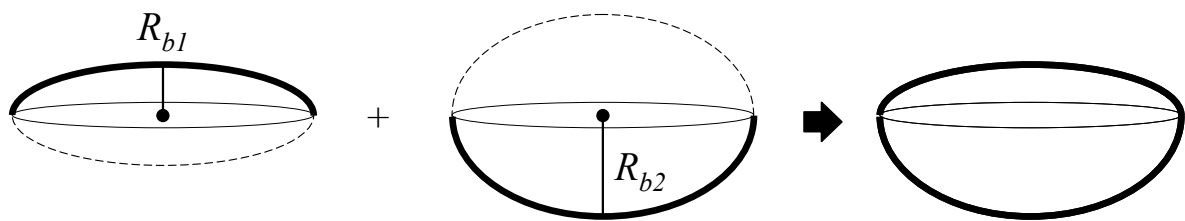


FIG. 4: Approximated bubble shape of a couple of half ellipsoids.

2.4. Program framework

For reducing computational time of the objects-objects interactions, each object has links to the neighbor objects. Figure 5 (a) describes the link structure. If there was no links as figure 5 (c), it has to calculate all surfaces at the searching step of the next cross point of a RAY and a surface. The link structure considerably reduces the number of the target surfaces as figure 5 (b) and thus reduces the computational time. The link structure is built as below; a BODY has information of its own ID (number) and SURFACE IDs which enclose the BODY itself. A SURFACE has information of its own ID and a couple of BODY IDs contacting the SURFACE. A RAY has information of its own ID and one SURFACE ID of the rooter, and one BODY ID holding the RAY itself.

Figure 6 shows the algorithm steps of the present ray tracing method. First, the calculation space and objects are rendered by BODY and SURFACE. Second, a number of RAYs irradiates the inlet tip (opposite to the sensing tip). In order to simulate the laser light source having a random linear polarization, every RAY's intensities are same and their position, direction and polarization angle are defined uniform randomly at the inlet tip. All objects of BODY, SURFACE and RAY are stored in their own database.

Third, the iteration step starts. The simulator selects a RAY which does not have its end point and calculates the nearest cross point of the RAY and SURFACES as the end point. Next, the refraction angle θ_r and reflection angle θ_i are calculated according to Snell's law. The reflectivity and the transmissivity are calculated by equations (6) - (9) and the reflected and refracted RAY objects are generated and are stored in the RAY database with the renumbered RAY IDs. The iteration will stop if all RAYs exited out of the calculation space or all branched RAY's energy decrease under a preset residue.

Forth and finally, the returned RAYs' energy is sum up at the inlet tip. The ratio of the returned RAYs' energy and incident RAYs' energy are defined as the probing signal of the numerical model. For reducing the coding cost and the calculation time, I developed the simulator engine in C language²², the running controller in bash script² and the visualization data in VTK file format²⁴.

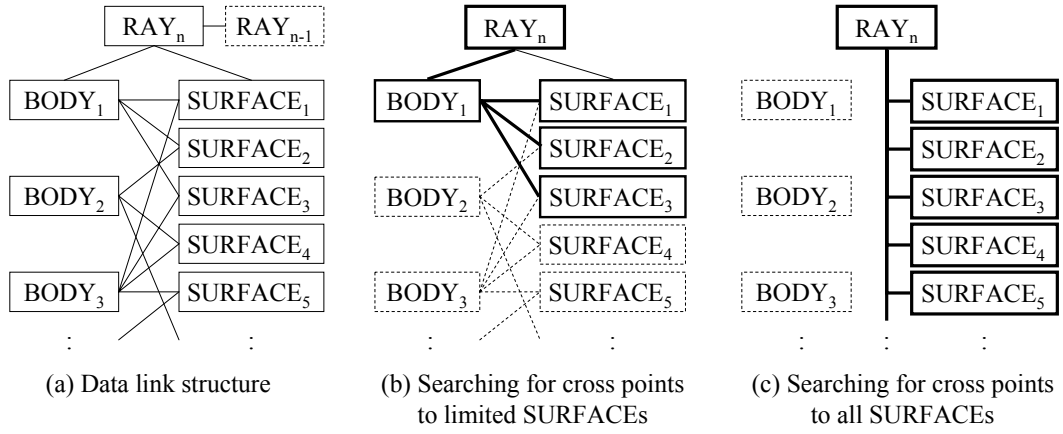


FIG. 5: Data link structure for reducing the calculation time

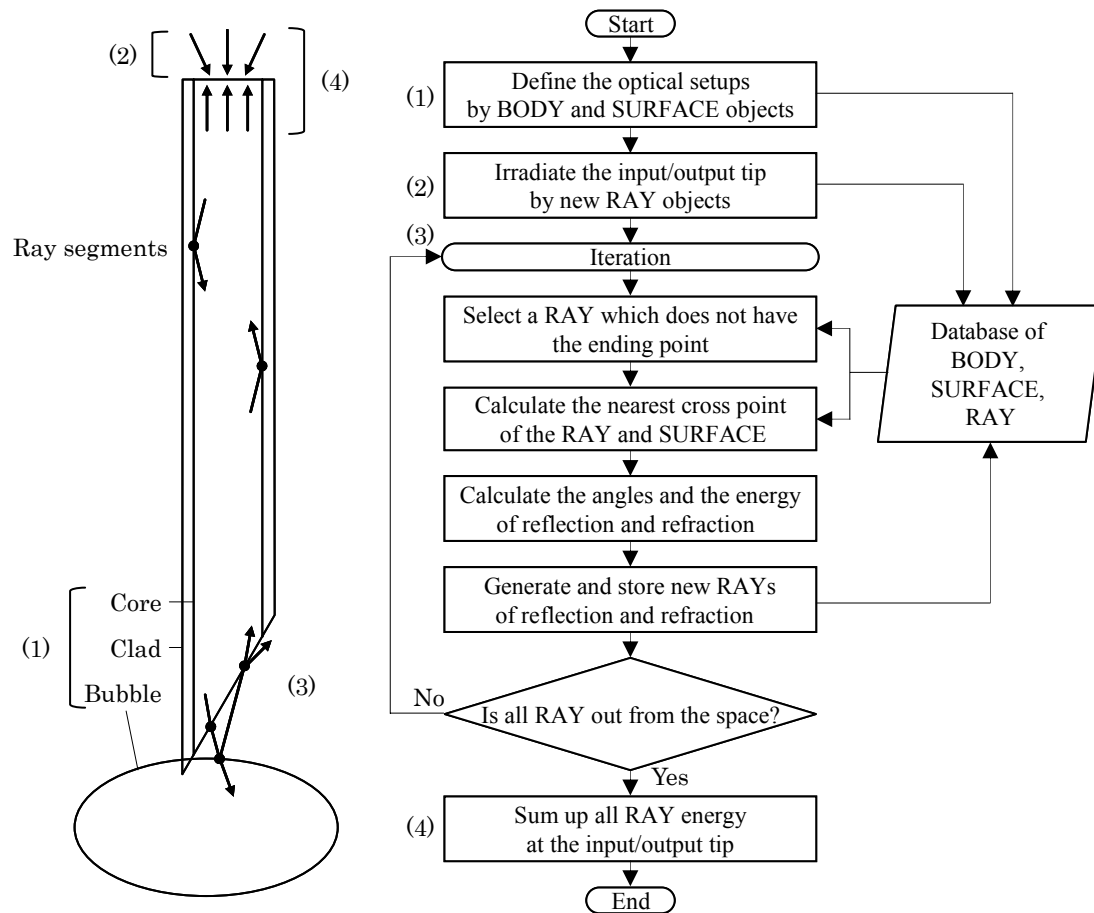


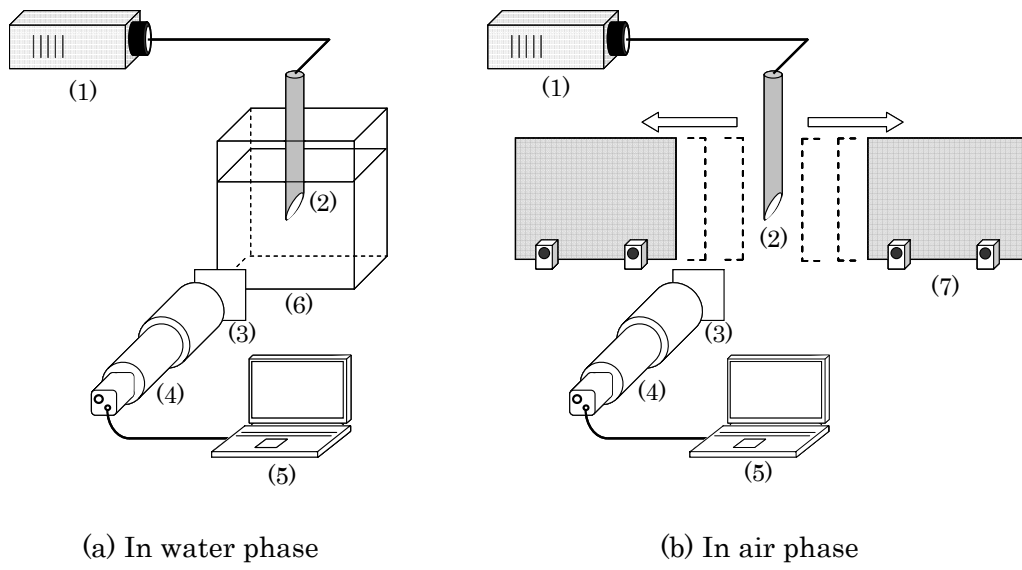
FIG. 6: Flowchart of the ray tracing method.

2.5. Experimental setups to verify the numerical model and analyze peak signals

I visualized the laser beam emission trajectories from the sensing tip. Figure 7 shows the visualization setup. It consists of a YAG-laser system (Elite, Laser Quantum, 532nm), an S-TOP (examined probe), a high-resolution CCD camera (WAT-902B, Watec, 720×480 pixels image, spatial resolution: 4.78 $\mu\text{m}/\text{pixel}$) with a sharp cut filter (SIGMA KOKI, SCF-50S-560, transmission limit wavelength: 560 nm). The source laser had a random linear polarization. The optical fiber composing the S-TOP was of a single mode step index type and the refractive indexes of its core and clad were 1.47 and 1.40, respectively. The outer diameters of its core and clad were 220 μm and 230 μm , respectively. The sensing tip was smoothly grounded in 35°.

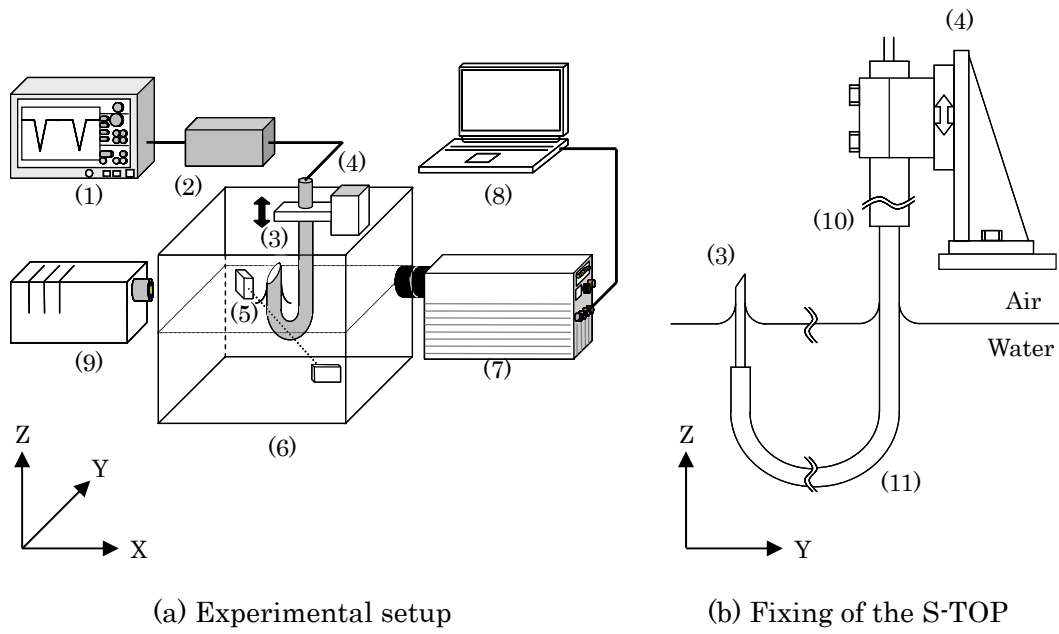
The beam trajectories from the sensing tip were investigated in both air phase (20 ± 1 °C) and water phase (20 ± 0.5 °C). In the water phase experiment, a solution of purified water and a very small amount fluorescent of rhodamine-B (6.2 mg/L, excitation wavelength: 535nm, fluorescence wavelength: 575 nm) was used. In the air phase experiment, a thin sheet which was sopped in rhodamine-B was moved incrementally in order to capture the light trajectory. After the experiment, the captured trajectory images were collaged in consideration of the positions in a computer graphic in order to make a whole visualized image.

Next, I investigated the probing signal when the S-TOP pierced a flat air-water interface. Figure 8 shows the optical setup of the experiment. It consists of a high-speed video camera (Fast cam, Photoron, 768×768 pixels, spatial resolution: 5.26 μm , shutter speed: 10000 frame/sec, the exposure time: 50 μsec) and the S-TOP which was the same as the previous and was mounted on a precision optical stage. The arm moved vertically by 5.0mm/s to pierce the static air-water interface, synchronized with the high-speed camera. The acrylic water vessel was filled with deionized and filtrated tap water and the water temperature was kept at 20 ± 0.5 °C. The temperature of the room air was kept at 20 ± 1 °C.



(1) YAG-laser, (2) S-TOP, (3) Sharp-cut filter,
(4) CCD camera, (5) PC, (6) Acrylic water
vessel, (7) Rhodamine-B sheet.

FIG. 7: Optical setup to visualize the beam emission trajectories from the sensing tip.



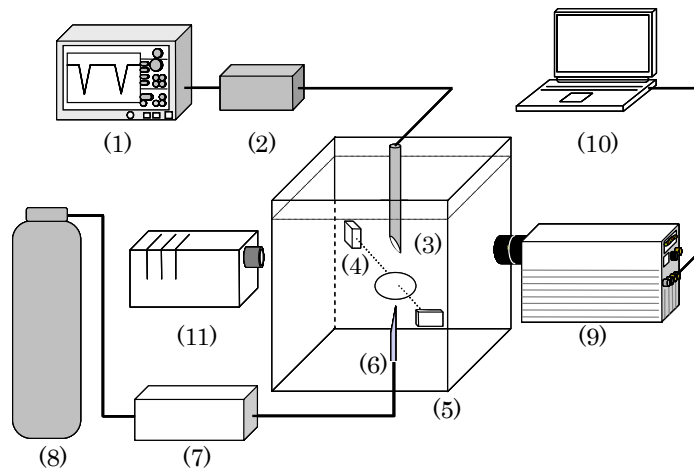
(1) Recorder, (2) Optical system, (3) S-TOP, (4) Motorized stage, (5) Optical sensor, (6) Acrylic water vessel, (7) High-speed video camera, (8) PC, (9) Halogen light source, (10) Stainless tube, (11) Stainless capillary.

FIG. 8: Optical setup to investigate the probing signal during penetrating the air-water interface from air to water or from water to air.

Next, I investigated the probing signal when the S-TOP pierced a bubble. Figure 9 shows the optical setup of the experiment which is almost same as the previous. A single bubble was launched from a hypodermic needle connected with a special bubble launch device (figure 10) composing an audio speaker, an audio amplifier, a function generator, an acrylic chamber and two precision pressure controllers¹⁹. The bubble volume was completely controlled by the launch device. The high-speed video camera (Fast cam, Photoron, 640×688 pixels, spatial resolution: 8.21 μm , shutter speed: 10000 frame/sec, the exposure time: 25 μsec) was synchronized with the data recorder (MEMORY HiCORDER 8861-50, HIOKI E. E., 100-kHz sample rate, 12-bit resolution). The water temperature was kept at 20 ± 0.5 °C. The temperature of the pure air supplied from the gas cylinder was kept at 20 ± 1 °C. The bubble shape was measured from the captured image and the bubble properties are listed in table 2.

Table 2: Bubble properties

Major axis	2.73	mm
Minor axis	1.52	mm
Equivalent diameter	2.08	mm
Rising velocity	0.295	m/s
Reynolds number	611	[-]
Eotvos number	0.582	[-]



(1) Recorder, (2) Optical system, (3) S-TOP, (4) Optical sensor, (5) Acrylic water vessel, (6) Hypodermic Needle, (7) Bubble launch device, (8) Purified air cylinder, (9) High-speed video camera, (10) PC, (11) Halogen light source.

FIG. 9: Optical setup to investigate the probing signal piercing a bubble.

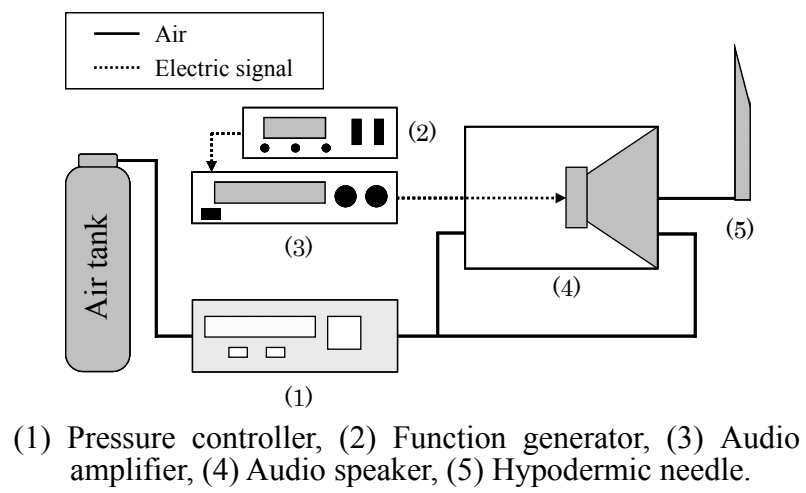


FIG. 10: Special-made bubble launch device.

2.6. Results and discussions

To analyze the probing signal of the S-TOP piercing an air-water free surface from an air phase to a water phase, I carried out the computations corresponding with the experiment described in the previous section. Figure 11 shows the visualized images of the beam trajectories emitted from the wedge-shaped tip. In the computation, 200,000 RAYs were installed at the inlet tip. The intensity range was so wide that each image was retouched for visibility; the bit depth of the computational images was expressed in a logarithmic intensity level. The experiment's images were collaged from 3 (in air phase) or 2 (in water phase) images. The 3 images of the air phase experiment were collaged from 30~43 incremental images.

I should note that it is very difficult to match the light intensity distribution between experimental image and numerical image. Because the experimental image gets the fluorescence intensity through several inevitable nonlinear conditions; i.e., deformative or roughness of optical fiber's surface, environmental light, scattered light, optical filters, and CCD noise. The nonlinearities become larger in the experiment in air. The numerical model does not simulate such nonlinearities. The images in figure 11 therefore should be compared based on the number of light beams and the directions of them.

Comparing each image, the computational results show a good accordance with the experiments. In particular, each direction of the strongest beam intensity of the computational results corresponds with them of the experiments. From these facts, the present numerical simulator is judged effectual for advanced analysis of the S-TOP signals.

I employed the numerical simulator to investigate the optimum angle of a wedge-shaped S-TOP for a high S/N ratio. Figure 12 shows the computationally obtained relation between the tip angle and the normalized intensity of the probing signal in the case that the wedge-shaped tip pierces an air-water interface from the water phase to the air phase by 2 mm above the interface. The computational result showed

three local maxima at around 30° , 45° and 90° . Figure 13 describes the reason why these angles enhance the probing signal; i.e. at the angles, incoming beams which are transmitted straightly to the sensing tip are reflected one to three times, in average, at the tip surface and returned straightly to the inlet tip. In the case of the other angles, after reflected many times, the incoming beams leak out much more from the optical probe. From a viewpoint of easily piercing a bubble, the recommended optimum angle is ranging from 28° to 32° computationally.

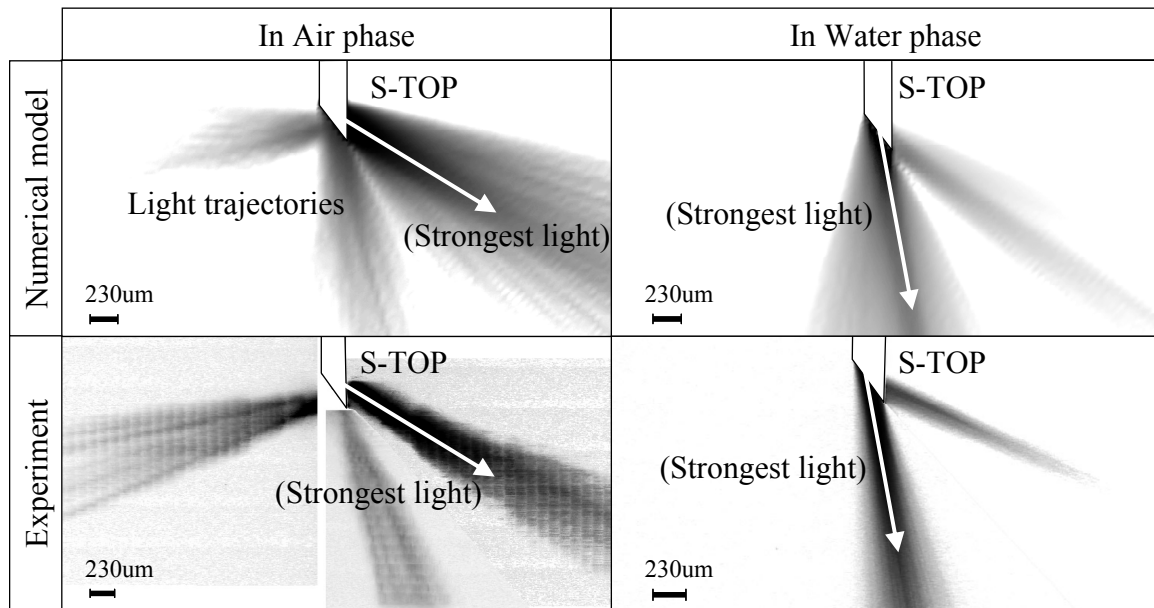


FIG. 11: Beam trajectories emitted from the wedge-shaped tip of the S-TOP.

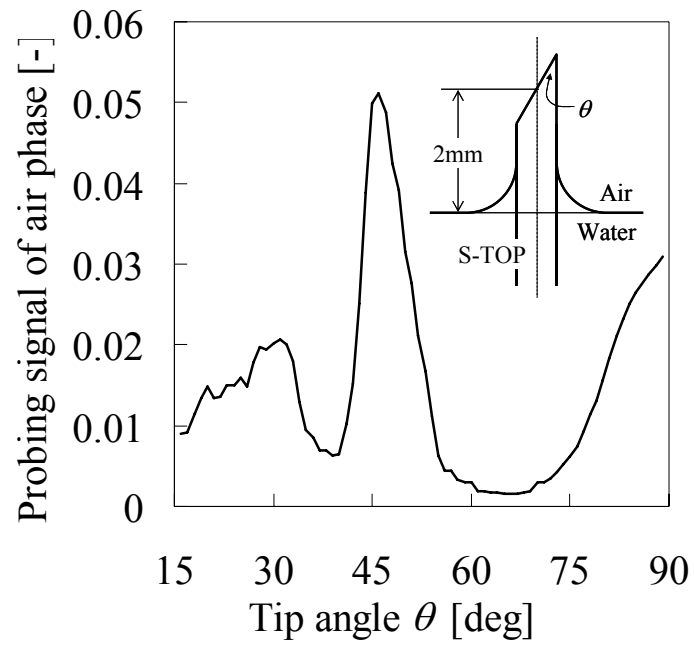


FIG. 12: Relationship of the tip angle and the probing signal of air

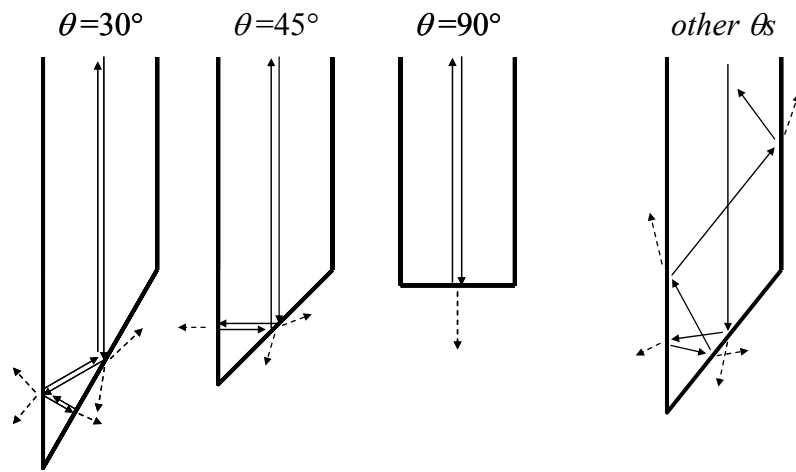
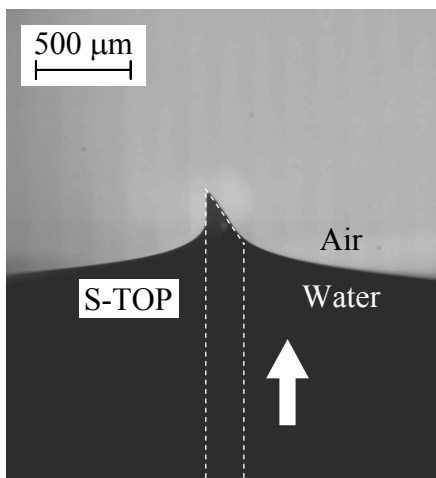


FIG. 13: Signal enhancement mechanism at the specific angles (30° , 45° , 90°) of the wedge-shaped tip.

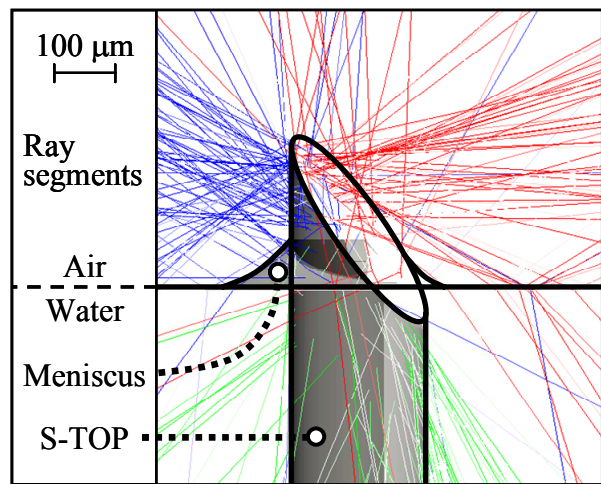
To analyze the probing signal of the S-TOP piercing an air-water free surface from an air phase to a water phase, I carried out the computations corresponding with the experiment described in the previous section. The left of figure 14 shows a snapshot of the S-TOP's piercing the interface from the water phase to the air phase. The right of the figure shows a typical visualization image of the computational results. The numerical meniscus radius was assumed to be ranged from 0.0mm (flat surface) to 0.4 mm which was considered to include the radius experimentally obtained from the visualization image in figure 14.

Figure 15 shows the probing signals of the experiments and the computations. The experimental results are the voltage of the photo-multiplier catching the returned ray from the inlet tip through the polarizer. In the case of the S-TOP piercing the interface from the air phase to the water phase, the computational results are well accorded with the experimental results. However, the experimental result from the water phase to the air phase differs from the computational result under a computational condition of a flat surface ($R_m = 0$, i.e. the interface is not deformed by the tip piercing). In order to improve the computational accuracy, I introduced a simple static meniscus model to consider the surface deformation, as described in the section 2.3.

The effects of the meniscus on the computational probing signal and the behavior of the rays with and without consideration of the meniscus are described in figure 15 (c). In the computational result without a meniscus (the left of figure 15 (c)), most rays which are concentrated at the wedge-shaped tip re-enter into the fiber and return to the inlet tip. In the corresponding result with a meniscus (the right of figure 15 (c)), some rays are directly emitted into the water phase, and thus the probing signal is depressed. As the result, the computational signal obtained with a 0.2-mm meniscus radius was in good accord with the experimental signal. The result also explains that the reflected light from an air-water interface and meniscus produce a pre-signal when a wedge-shape optical fiber probe pierces the interface.

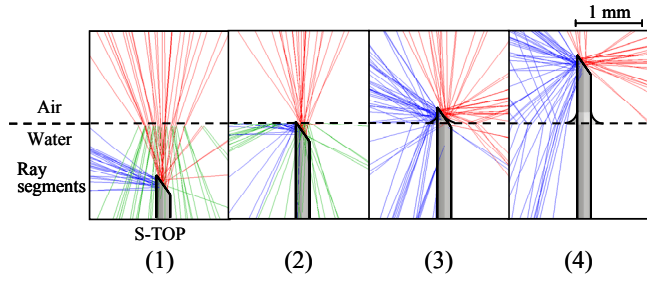
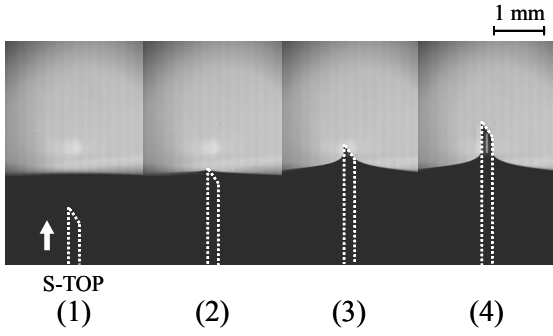
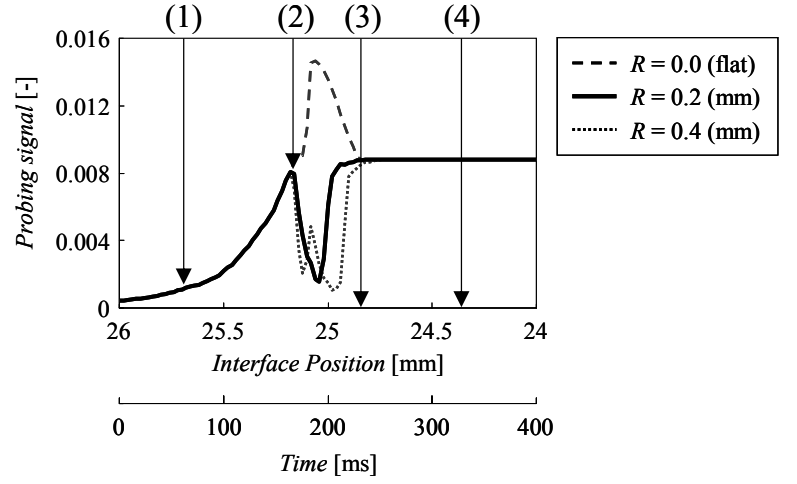
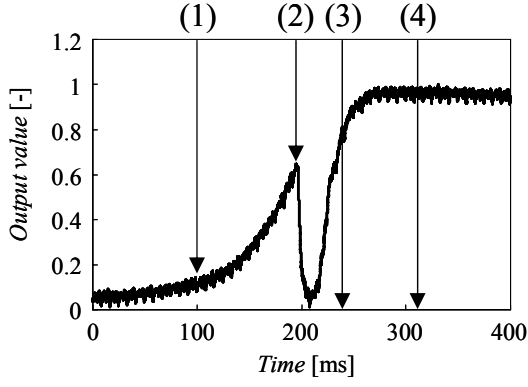


(a) Experiment



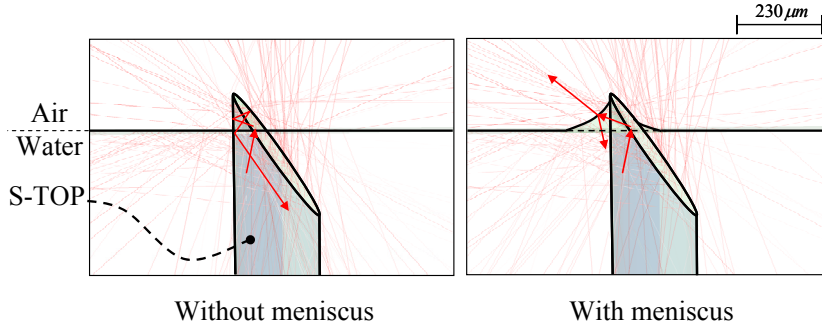
(b) Numerical simulation

FIG. 14: Visualization of a probe piercing an air-water interface.



(a) Experiment

(b) Numerical simulation



(c) Intermediate position of (2) and (3) (Interface position = 25.06 mm).

FIG. 15: Probing signals of the S-TOP piercing a free surface.

220 μm in core diameter, 5 μm in clad thickness and 35 degrees in wedge angle. (a) Experimental results. (a-1) Normalized probing signal by experiment. (a-2) Snapshots of the piercing process corresponding to the event time in the probing signal. (b) Computational results. (b-1) Normalized probing signal by computation. (b-2) Computational rays; red lines: discharged rays from the wedge-tip surface, blue lines: discharged rays from the side of the wedge-shaped tip, and green rays: reflected rays on water-air interface. (c) Intermediate position of (2) and (3) (Interface position = 25.06 mm).

Figure 16 shows time-series snapshots during the S-TOP's penetration of a bubble frontal interface obtained from the high-speed visualization in the experiments. Figure 18 shows the experimental probing signal obtained from the experiment of figure 16. It shows a pre-signal appears clearly.

Figure 17 shows the visualization of the computational beam trajectories under the same bubble positions as the experimental ones. The numerical bubble—the major axis and minor axis of which were the same as those of the bubble in the experiment—was modeled out of two half-ellipsoids (as shown in figure 4). The center axis of the bubble agreed with the fiber axis. This figure shows that the probing signal can take two peaks; i.e., figure 17(2) shows a bundle of RAYs returning from the bubble rear interface to the sensing tip due to reflection via a concave-mirror effect of the rear interface. In addition, figure 17(3) shows that another bundle returns from the bubble frontal interface successively. I identified a new mechanism of the pre-signal based on the computational analysis.

Figure 19 shows the computed probing signals when penetrating the ellipsoidal bubble; i.e., $R_{b1} = R_{b2}$ and the meniscus radius R_m was changed from 0.0 to 0.4 mm. Two thousand RAYs were installed at the inlet tip. The bubble position numbers (1–4) correspond to those in figures 17 and 18. In figure 19, the second pre-signal clearly appears at bubble position (3). Indeed, this result reveals a new mechanism of the pre-signal.

Figure 20 shows the computed probing signals when the S-TOP penetrated a dissymmetric and deformed ellipsoidal bubble; i.e., the radii ratio R_{b1}/R_{b2} was changed from 0.4 to 1.2, but the minor axis ($R_{b1} + R_{b2}$) and the meniscus radius R_m were fixed as 1.36 mm and 0.2 mm, respectively. Figure 20 shows that the larger R_{b2} (the shorter curvature of the bubble rear interface) gives the shorter time between the first pre-signal at the position (2) and the sensing-tip contact with the bubble frontal interface. The figure reveals that the first pre-signal is caused by focusing the beams from the rear

interface like a concave mirror, and that the second pre-signal is caused by direct reflection from the bubble frontal surface. The pre-signals therefore appear only in the scenario in which the wedge-shaped tip pierces the center of a bubble. This phenomenon can be used to determine whether the tip pierced the center area of a bubble, and therefore it will contribute to advanced bubble/droplet measurement.

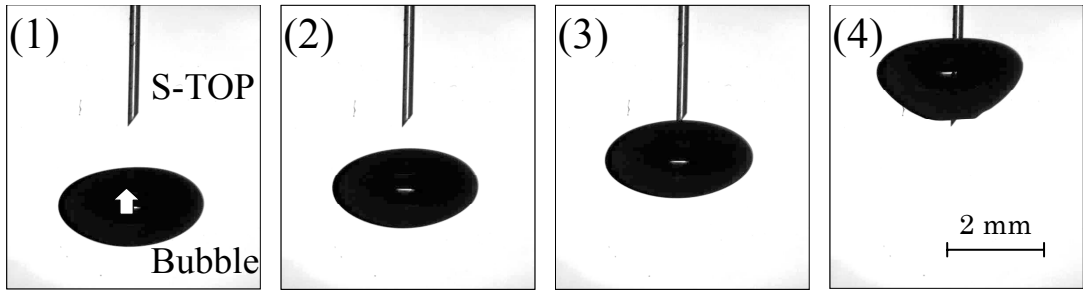


FIG. 16: High-speed video images of a S-TOP piercing a bubble.

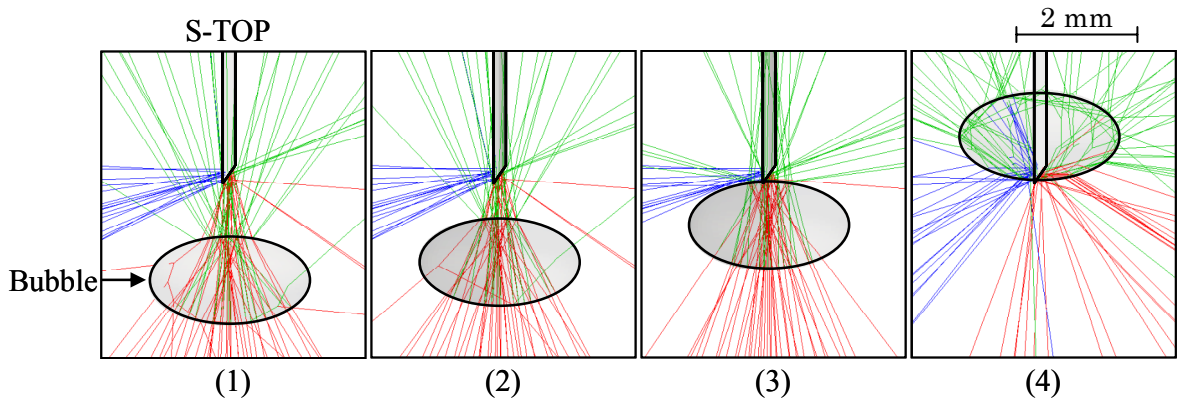


FIG. 17: Computational results of ray tracing analysis in the S-TOP piercing a bubble. red lines: discharged rays from the wedge-tip surface, blue lines: discharged rays from the side of the wedge-shaped tip, and green rays: reflected rays on the bubble interface. The figure numbers correspond to those in FIG. 19.

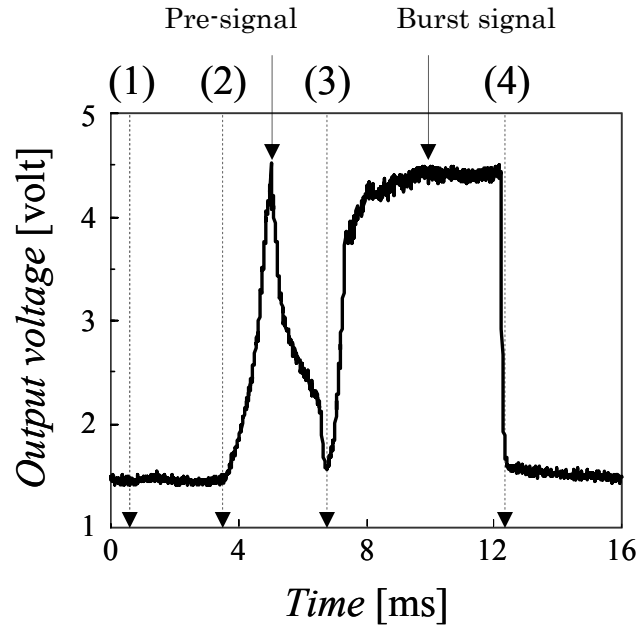


FIG. 18: Probing signal during the S-TOP piercing a bubble (experiments).

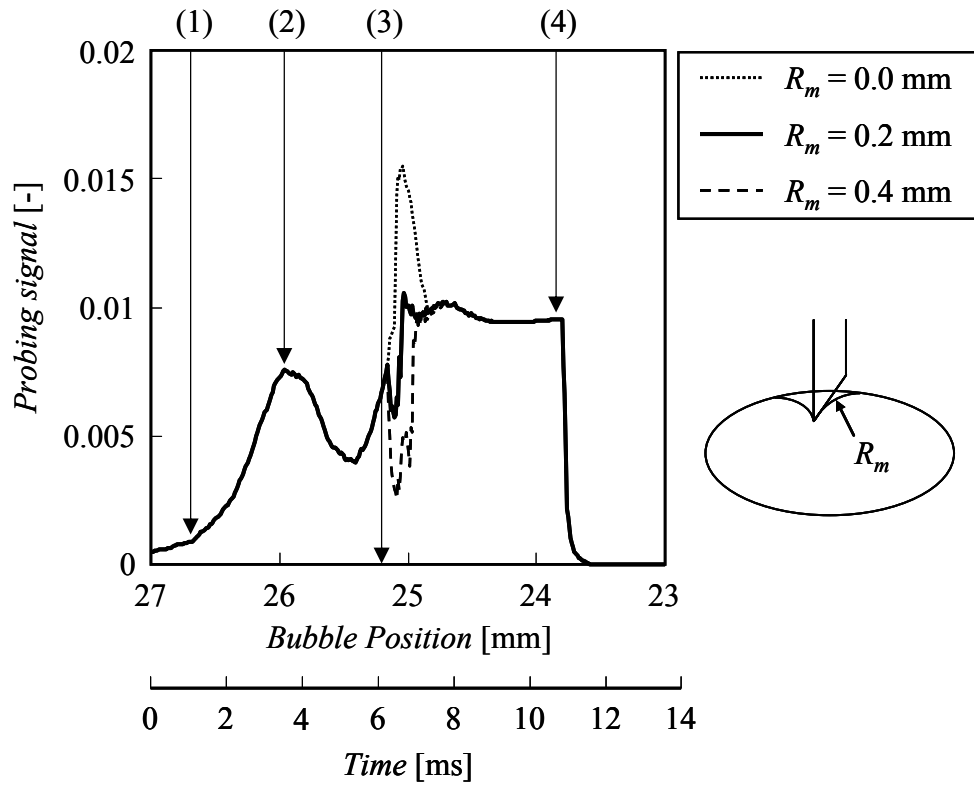


FIG. 19: Probing signal during the S-TOP piercing a bubble (computations).

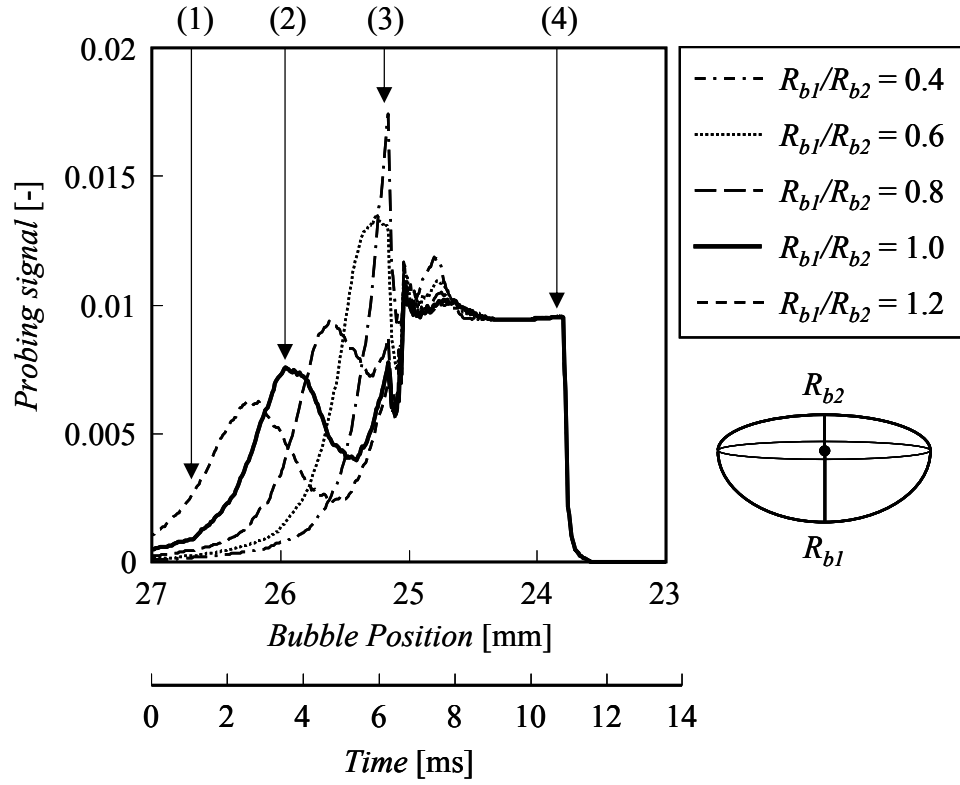


FIG. 20: Probing signal in consideration of bubble shapes during the S-TOP piercing a bubble (computations).

2.7. Conclusion

I developed an optical fiber probing simulator based on ray tracing algorithm in order to reveal mechanisms of some promising signals of an optical fiber probe, for the future advanced measurement. In the simulator, the rays' energy is calculated precisely based on Fresnel's law, furthermore, the whole optical phenomena (i.e., the incident beams, the emitted beams from the sensing tip, the beams reflected and refracted on the air-water interface, the beams re-entered into the sensing tip and beams transmitted through the optical fiber) is calculated in three-dimension. Analyzing probing signals of the S-TOP under some optical conditions computationally, I revealed the following mechanisms:

(1) The optimum angle of the sensing tip for the S-TOP.

Calculating the emitted-beam trajectories from the sensing tip of the S-TOP (Single-Tip Optical-fiber Probe with a wedge-shaped sensing tip), the computational results were well accorded with the experimental results. I obtained the optimum angle of the wedge-shaped probe as $30^{\circ} \pm 2^{\circ}$.

(2) The relation between an interface deformation and the probing signal.

Calculating the signals output from the S-TOP piercing an air-water flat interface, I pointed out the interface deformation affected the probing signals. Under a numerical condition of no deformation of the interface, the calculated signal showed an intensive peak just when the sensing tip touched the interface; this was caused by direct reflection from the interface. Under a numerical condition of a 0.2 mm meniscus radius, the calculated signal was well accorded with the experimental signal.

(3) The mechanism of the pre-signals.

The pre-signals were considered to be caused by the reflected beams from the frontal and rear surfaces of the bubble. The peak time was changed in association with the curvatures of the bubble frontal and rear surface. These phenomena are hopeful for the future advanced measurement.

3. Automatic detection of phase signal levels from raw probing signal

3.1. Problems of conventional algorithm

The basic algorithm consists of several steps to quantify the bubble properties of velocities, diameters and void fractions from the raw probe signals as shown in figure 21. In the first step, the air level V_{Air} [-] and water level V_{Water} [-] are determined from the raw signals. In the second step, the signals are transformed into trapezoidal waveforms. In the third step, the event times of the air-water phase switching are determined. In the fourth step, bubble diameters (or pierced chord lengths in a strict sense), velocities and number density, and point-wise time-based void fractions are calculated. As described above, the determination of air and water levels (the first step) is very important and significantly influences the subsequent processes and the results.

The conventional min-max method does not effectively work in processing noisy signals, for example, industrial bubble measurements. Hence, I developed a new histogram method and median method. Details of these methods are discussed in section 3.2.

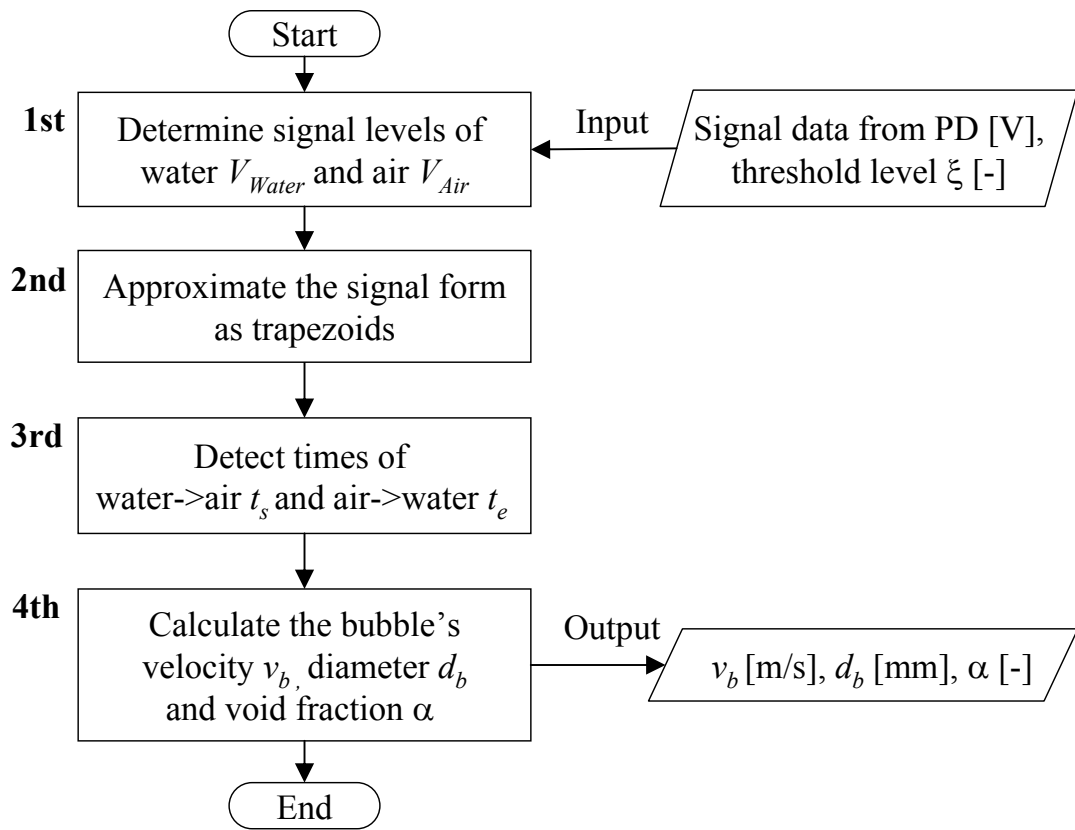


FIG. 21: Algorithm overview.

The min-max method is a simple algorithm. In this method, the air level V_{Air} [-] and water level V_{Water} [-] are analyzed by the following steps:

- Detecting the maximum level V_{Max} [-] and minimum level V_{Min} [-] of the signal.
- Defining the threshold level V_{th} [-] using the preset threshold parameter ζ [-] as

$$V_{th} = \zeta(V_{Max} - V_{Min}) + V_{Min}, \quad (10)$$

where the preset parameter ζ [-] ranges from 0 to 1.

- Detecting the air level V_{Air} as the average of the data larger than the threshold V_{th} , and the water level V_{Water} as the average of the data smaller than the threshold V_{th} .

This algorithm requires the preset parameter ζ , which must be given before the calculation. The calculation results of V_{Air} and V_{Water} inevitably depend on the vague parameter of ζ . In industrial use, the appropriate range of ζ is usually very narrow and tends to fluctuate. This problem results in decreased measurement accuracy. The relations between ζ and both V_{Air} and V_{Water} are discussed in section 3.3.

3.2. Algorithms to precisely and rationally detect phase signal levels

The histogram method is a more robust algorithm than the min-max method. Figure 22 shows the principle of the algorithm. The histogram method is able to distill the peaks corresponding to the air level, water level and other useful phenomena.

The algorithm is executed by the following steps:

- Determining the histogram of the probing signal.
- Detecting the water level V_{Water} as the first peak of the histogram and the air level V_{Air} as the second peak of the histogram.

This algorithm requires the preset parameter n [-] of the histogram resolution. This has two problems as described in figure 23; i.e. (1) if the resolution n is too low, the accuracy of V_{Air} and V_{Water} degrades significantly; (2) conversely, if the resolution n is too high, the histogram will have many peaks, making it difficult to extract V_{Air} and

V_{Water} . Details of the relations between the histogram resolution n and V_{Air} and V_{Water} are discussed in the next section.

In order to solve the histogram resolution problem and obtain proper and meaningful peaks, I developed the median method which uses median values instead of the values directly obtained from the histogram shape. The algorithm steps are as follows:

- Detecting the water signal level V_{Water} as the median value from the raw signal. (figure 24 (1))
- Detecting the air signal level V_{Air} by the following steps:
 - Picking out data larger than $(V_{Water} + k\sigma)$ from the raw signal. (Figure 24 (2)), where σ [-] represents the standard deviation of all raw signal data and k [-] is a preset parameter.
 - Detecting the air signal level V_{Air} as the median value from the picking-out signal. (Figure 24 (3))

This algorithm has two advantages. (1) No preset parameter is needed for detecting V_{Water} . (2) The preset parameter k for detecting V_{Air} is not sensitive to noise. The relation between k and V_{Air} is discussed in the next section.

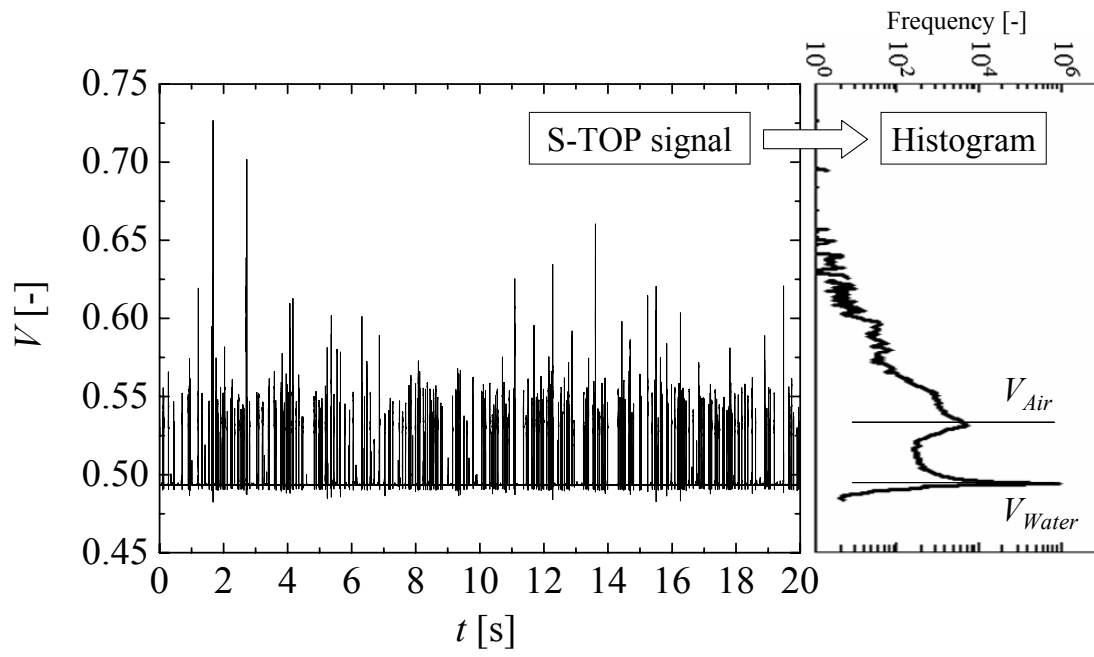


FIG. 22: Making a histogram from the S-TOP signal for detecting the air / water levels.

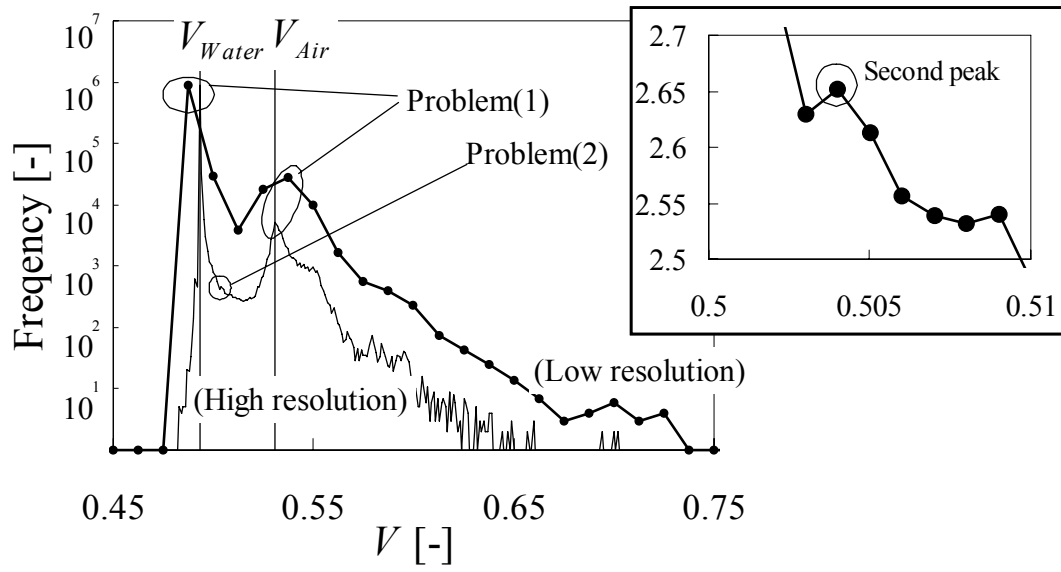


FIG. 23: Problems of detecting the unique peak of a histogram:
 (1) low resolution depresses the measurement accuracy,
 (2) split-peaks interfere with the determination of the second peak.

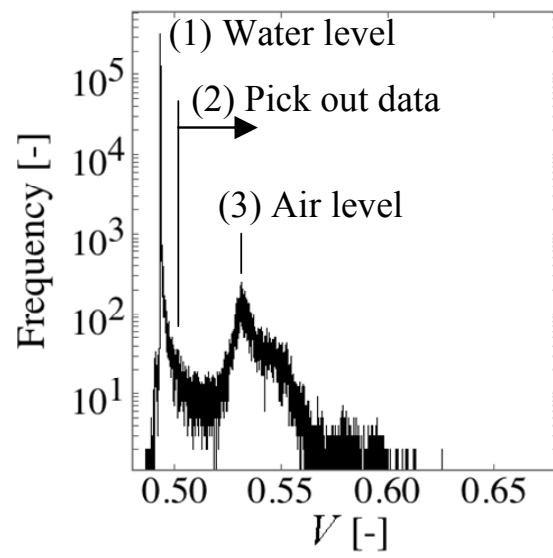


FIG. 24: Algorithm steps to detect air/water levels from two median values.

3.3. Experimental results and discussions

The relations between the preset parameters (ζ , n , k) and the accuracy of these three algorithms were observed via sample signals. The signals were obtained arbitrarily by a four-tip optical fiber probes (F-TOP) from the experiments described in chapter 4.

Figure 25 shows their raw signals in the upper row and histograms in the lower row. The center probe's histogram (a) shows a clear S/N ratio; in other words, the air level V_{Air} and the water level V_{Water} are sufficiently separated. By contrast, the outer probe's histograms (b) and (c) show a poor S/N ratio.

This difference is estimated to be caused by the positions of these probes. The center probe sticks out from the outer probes and pierces bubbles directly, while the outer probes do not. Therefore, when a bubble is pierced by the center probe, it keeps its original shape for the most part. In contrast, when the bubble is pierced by the outer probes, it has already touched to the center probe and its shape is often deformed more than when it is pierced by the center probe. The bubble deformation decreases the S/N ratio.

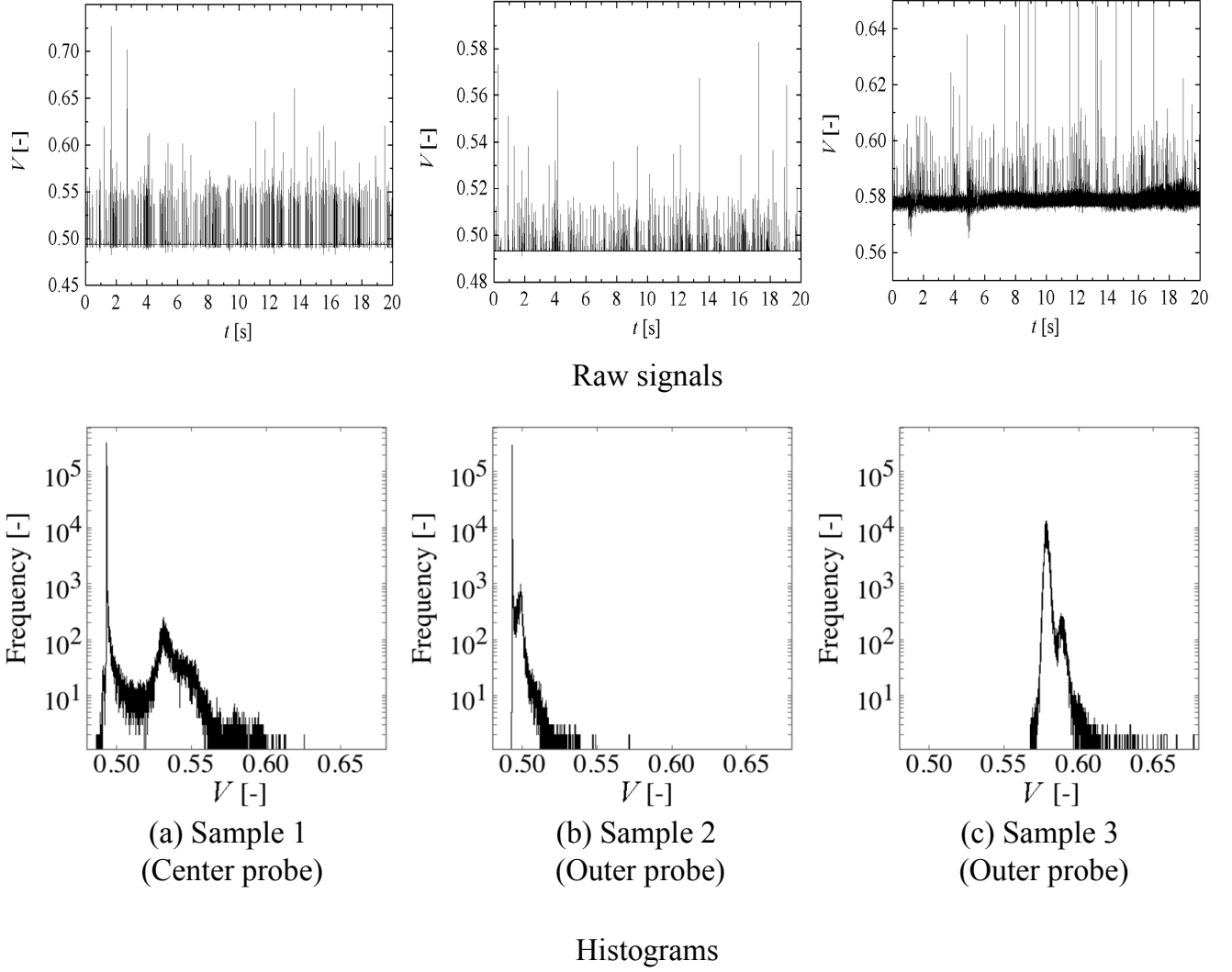


FIG. 25: Raw signals and histograms of sample signals from an F-TOP.

As the result, in the signal (b) and (c) it seems more difficult to determine the air level V_{Air} and the water level V_{Water} especially by the conventional min-max method. The detected V_{Air} and V_{Water} from the same dataset as used in figure 25 by the min-max method are shown in figure 26. The horizontal axis is the parameter ζ and the vertical axis is the difference in detected signal levels between the min-max method and the median method ($k = 2$).

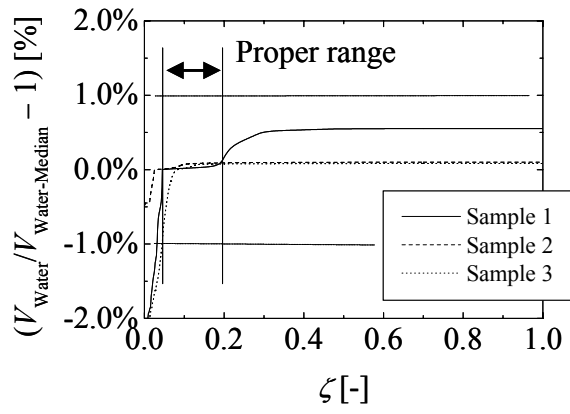
The reason why I used the median method outputs as the reference of the comparison is there are no other independent methods to decide air/water signal levels automatically. Before figures 26-28, I confirmed the outputs of median method were corresponded well with the peak positions of histograms in figure 27. Furthermore, I confirmed again each algorithm with PIV method in bubble velocity measurement in section 4.4 and concluded the median method was most successful.

The results indicate that these levels highly depend on the preset parameter ζ , especially for V_{Air} . The proper value for ζ ranges from 7.5 % to 9.5 %. The range is too narrow and unpredictable because the calculation is easily changed by the occasional spike peaks in the raw signals. Predicting the proper range before analyzing is therefore difficult or impossible. This results in the complexities and uncertainties of the min-max method.

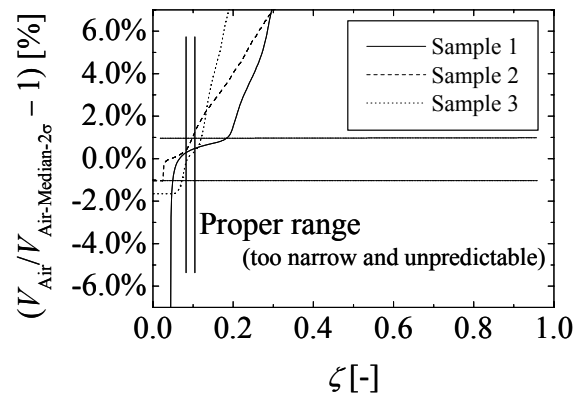
The air level V_{Air} and water level V_{Water} detected by the histogram method from the same dataset in figure 25 are shown in figure 27. The horizontal axis is the histogram resolution n and the vertical axis is the differences of detected signal levels between the histogram method and the median method. The histogram method has much more robustness than the min-max method. The proper value of n ranges from 600 to 2000. Generally, 1000 is the proper value of the histogram resolution.

The histogram method has satisfactory robustness; the median method is still more robust. The median method decides a unique water level V_{Water} without any preset parameters. The preset parameter k is needed when the air level V_{Air} is calculated.

Figure 28 shows the air level V_{Air} detected by the median method. The horizontal axis represents the preset parameter k and the vertical axis represents the difference between the detected signal levels V_{Air} and $V_{Air-2\sigma}$ ($k = 2$) when both are calculated by the median method. The proper range of k takes 1.0 to 3.0 for all samples, and the best value is $k = 2.0$.

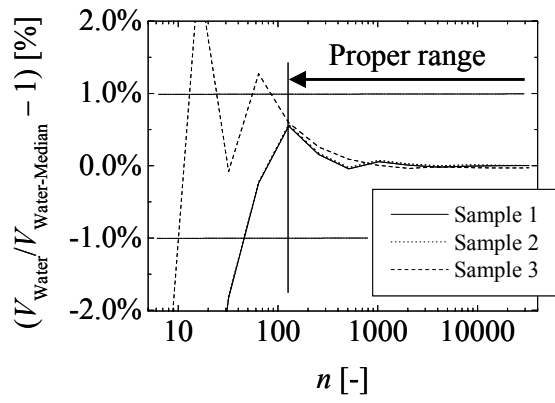


(a) Water level

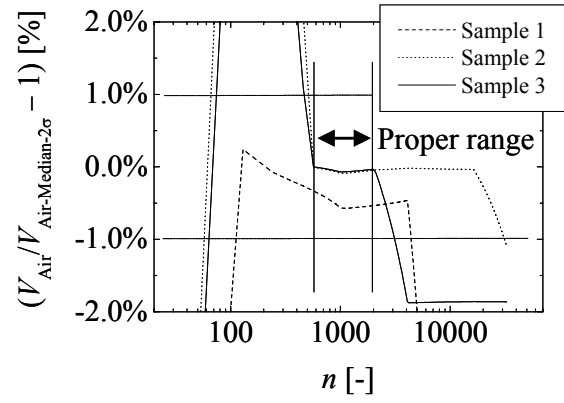


(b) Air level

FIG. 26: Proper range of the parameter ζ in min-max method.



(a) Water level



(b) Air level

FIG. 27: Proper range of the parameter n in histogram method.

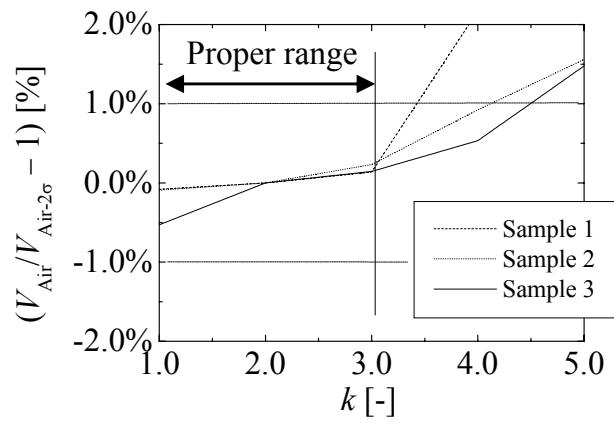


FIG. 28: Proper range of the parameter k in median method.

I analyzed the performances of the min-max method, histogram method, and median method in practical use by a sample flow in the bubble column shown in figure 37. The conditions of the sample flow are as follows: the measured height was 4250 mm from the air injection (F-TOP7), the air injection rate was 0.20 Nm³/min, the average velocity of bubbles is 0.48 m/s. The PIV method was applied for comparison. The image capture rate was 30 fps, and the captured image size was 135mm in 540 pixels.

The average uncertainty of the velocity was

$$\frac{135mm / 540pixel}{0.48m / s \times (1/30)s} = 1.6\% . \quad (11)$$

The measurement conditions for the F-TOP7 were as follows: the sampling rate of the data recorder was 50kHz, and the sampling time was 20 seconds. The preset parameters were $\zeta = 0.075$ for the min-max method, $n = 1000$ for the histogram method, and $k = 2.0$ for the median method, respectively. The threshold level ζ_{Water} was set as 0.35 for all the methods.

Figure 29 shows the histogram of the bubble velocity for each of the 4 measurements and table 3 summarizes the performances. The histogram and median methods show good similarity with the PIV results. However, the min-max method does not agree with them due to the excessively small number of detected bubbles. In practical use of the F-TOP measurement, despite removing the background noise in the settings, the conventional min-max method was not successful. While both the histogram and median methods were satisfactorily successful, the latter was found to be the best.

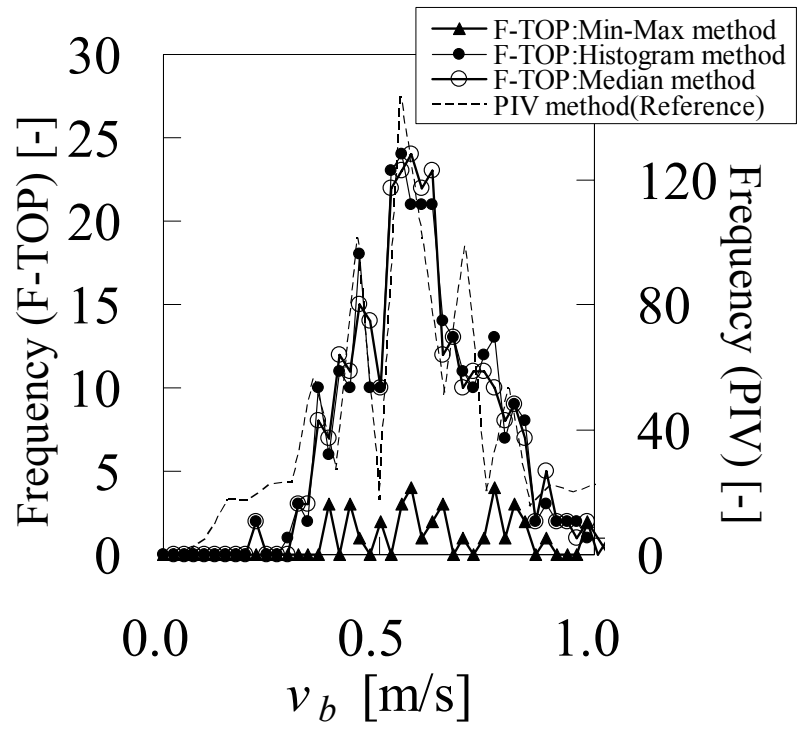


FIG. 29: Histogram of the detected bubble velocity.

Table 3: Comparison of average velocity and detected bubbles

Method		Average velocity [m/s]	Difference [%]	Detected bubbles [-]
F-TOP	Min-Max	0.441	-9.0	40
	Histogram	0.462	-4.6	305
	Median	0.464	-4.3	306
PIV (Reference)		0.485	⌵ (compared to PIV)	

3.4. Conclusion

Optical fiber probing in industrial measurements often includes inevitable peak signals which depress the stability of the signal processing. I therefore developed new robust signal-analyzing algorithms to detect the air/water phase level; histogram method and median method. Compared with the conventional algorithm of min-max method, the new algorithms showed a high level of robustness in analyzing sample signals obtained from industrial-scale bubble column experiments. I proposed the recommendation range of the preset parameters of n (resolution of the histogram method) from 600 to 2,000 and k (in median method) from 1.0 to 3.0 for reliable measurement.

4. Industrial bubble flow measurement

4.1. Measurement principle of F-TOP

The S-TOP measures the time-based local void fraction, the bubble diameters and the velocities parallel to the probe's optical axis, simultaneously³⁷. A Four-Tip Optical fiber Probe (F-TOP) expands the measurement ability. The F-TOP measures the bubble velocities and diameters in consideration of the directions of the bubble motions and orientations. Figure 30 illustrates the basic structure of the F-TOP. F-TOP easily and precisely recognizes bubble or droplet diameters and the velocities in three dimensions by assembling the sensing edges of the four S-TOPs in a triangular pyramid^{27,29}. The center fiber probe is positioned at the center of the equivalent triangle, and the outer probes are positioned at the apexes. The gap between the center probe and outer probes h_2 was 1 mm, and the clearance between the center probe and each outer probe h_1 was 0.25 mm, based on the geometrical relation between F-TOP and the bubbles examined in the demonstration. Details of the measurement algorithm by the F-TOP are explained in the following section.

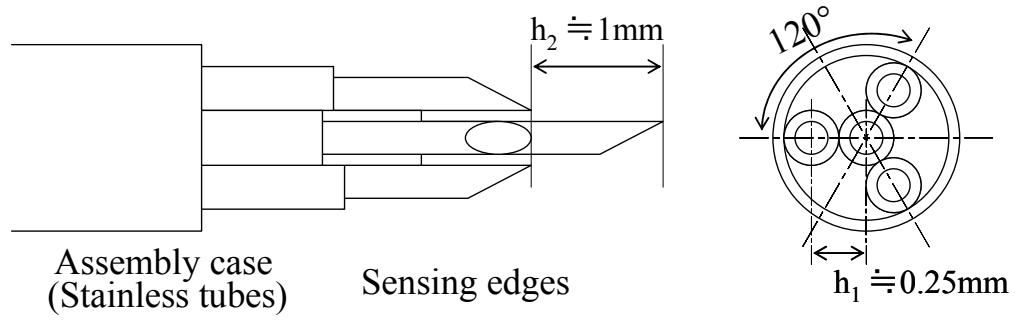


FIG. 30: Basic structure of F-TOP.

4.2. Algorithm to detect bubbles' velocity, diameter and void fraction

Figure 31 outlines a flowchart of the F-TOP measurement. At the first step, the histogram method is applied, and the air level V_{Air} [-] and the water level V_{Water} [-] are detected.

Figure 32 explains the second step in detecting the event times of air-water switching. The details are:

- Define a pair of thresholds th_{Water} [-] and th_{Air} [-] between V_{Air} and V_{Water} by using the preset threshold parameters ξ_{Water} [-] and ξ_{Air} [-],

$$th_{Water} \equiv \xi_{Water}(V_{Air} - V_{Water}) + V_{Water}, \quad th_{Air} \equiv \xi_{Air}(V_{Air} - V_{Water}) + V_{Water}, \quad (12)$$

where $0 < \xi_{Water} < \xi_{Air} < 1$.

If the air and water levels V_{Air} and V_{Water} are determined with sufficient accuracy, the proper values of the parameters are $\xi_{Water} = 1/3$, $\xi_{Air} = 2/3$.

The phase changes from water to air are judged when the signal increases, crossing both th_{Water} and th_{Air} . Conversely, when the signal decreases, crossing both th_{Air} and th_{Water} , the phase change from gas to liquid is judged. When the signal crosses only th_{Water} and th_{Air} , it is neglected as an invalid penetration, and the analysis proceeds to the next step.

- Connect the cross points of the signal crossing th_{Water} and th_{Air} by straight lines.
- The cross points of the approximated line and water-level line of V_{Water} are defined as the event times; i.e., the first cross point t_s [s] means the time when the sensing tip starts to enter a bubble, and the second cross point t_e [s] means the time when the sensing tip exits from the bubble.

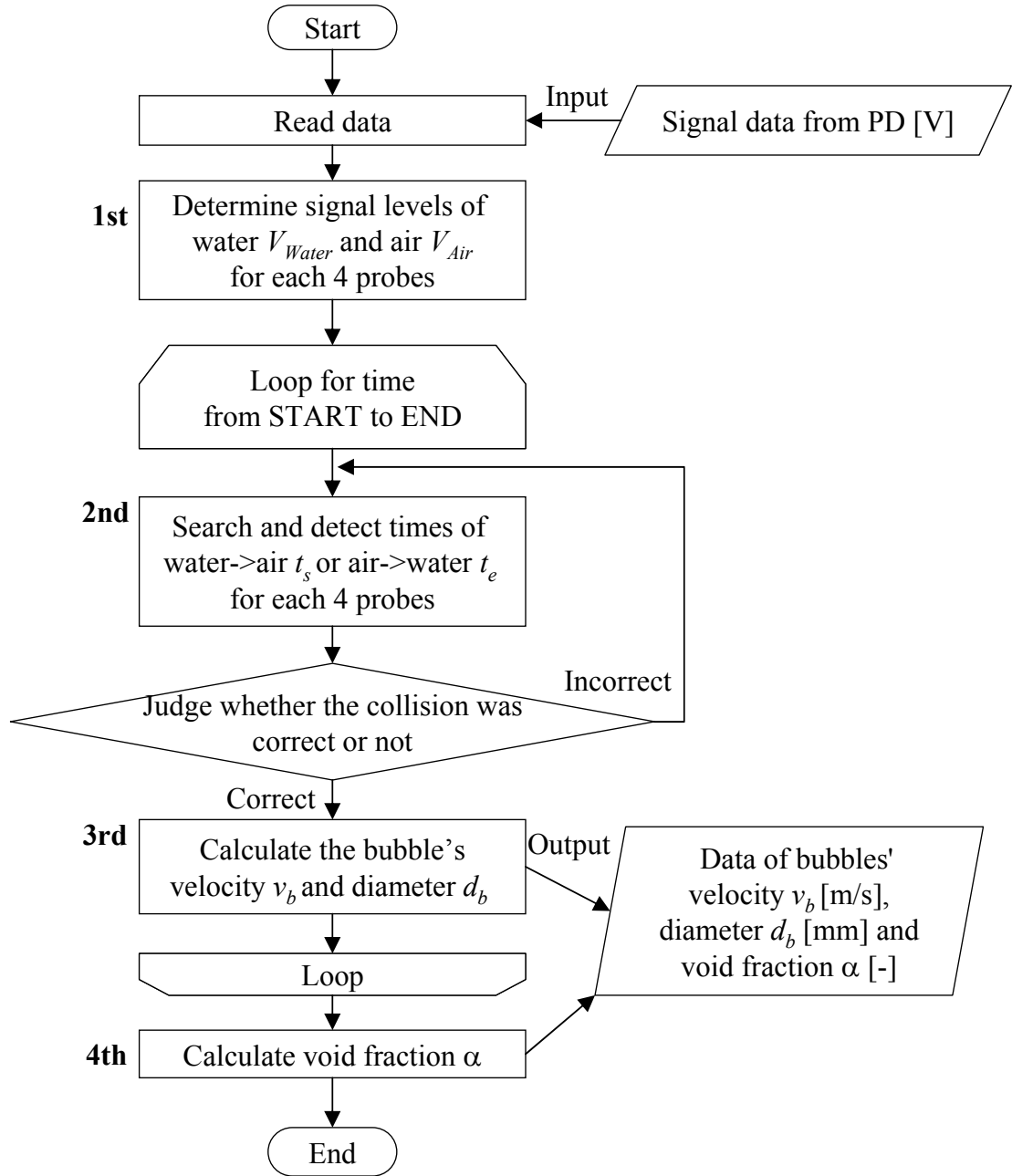


FIG. 31: Flowchart of the signal analysis algorithm for the F-TOP.

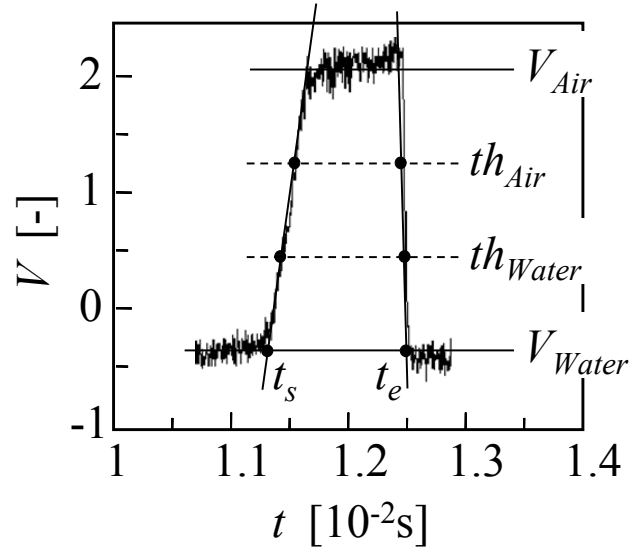


FIG. 32: Detecting the event times

At the third and the fourth steps, the bubble velocity \mathbf{v}_b [m/s] = (v_b, θ_v, ϕ_v) , pierced chord length d_{bs} [m] and time-based void fraction α_{time} [-] are calculated by equations (13) – (19).

The bubble velocity \mathbf{v}_b is obtained from the differentials between the F-TOP sensing edges and the frontal surface of the bubble. To evaluate the \mathbf{v}_b , Xue proposed implicit equations⁴⁸. The equations are useful, however, the software need optimization solver which depress the analyzing performance. I therefore derived explicit equations under an approximation; i.e., the sensing edges comprise a triangular pyramid, the frontal surface is assumed to be a flat plane, the velocity \mathbf{v}_b is assumed to be constant during the penetration, and the direction of \mathbf{v}_b is assumed to be parallel to the normal vector of the plane. In these assumptions, a collision of the probe and a bubble's frontal surface is approximated as a collision of four vertices of a triangular pyramid and a flat plane, as shown by figure 33.

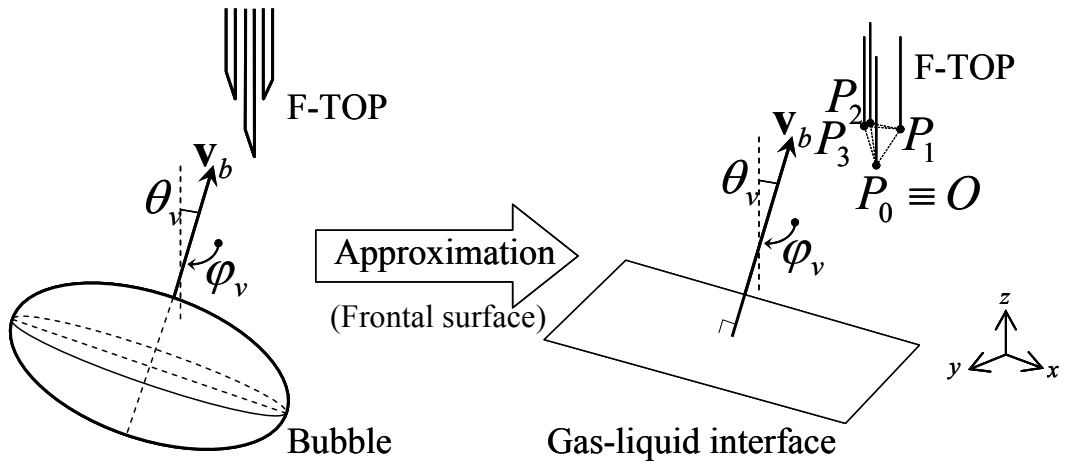


FIG. 33: Approximation of probe-bubble contact.

Supposing the coordinate of the center probe tip \mathbf{P}_0 [m] as the origin, the coordinates of the outer probe edges $\mathbf{P}_1, \mathbf{P}_2, \mathbf{P}_3$ [m] are defined as:

$$\begin{pmatrix} \mathbf{P}_1 \\ \mathbf{P}_2 \\ \mathbf{P}_3 \end{pmatrix} \equiv \begin{pmatrix} h_1 & 0 & h_2 \\ -\frac{1}{2}h_1 & \frac{\sqrt{3}}{2}h_1 & h_2 \\ -\frac{1}{2}h_1 & -\frac{\sqrt{3}}{2}h_1 & h_2 \end{pmatrix}. \quad (13)$$

The bubble's velocity vector \mathbf{v}_b is supposed as

$$\mathbf{v}_b \equiv v_b \begin{pmatrix} \sin \theta_v \cos \varphi_v \\ \sin \theta_v \sin \varphi_v \\ \cos \theta_v \end{pmatrix} = v_b \mathbf{n}_s, \quad (14)$$

where \mathbf{n}_s [-] is a normal unit vector of the flat plane.

Supposing the contact time t_{s0} of the \mathbf{P}_0 and the flat plane is 0 second, the contact times t_1, t_2, t_3 [s] of the edges $\mathbf{P}_1, \mathbf{P}_2, \mathbf{P}_3$ and the flat plane are derived as:

$$v_b \begin{pmatrix} t_1 \\ t_2 \\ t_3 \end{pmatrix} = \begin{pmatrix} \mathbf{P}_1 \\ \mathbf{P}_2 \\ \mathbf{P}_3 \end{pmatrix} \mathbf{n}_s. \quad (15)$$

From the equation, the components of \mathbf{v}_b are derived as follows:

$$v_b = \frac{3h_2 \cos \theta_v}{t_1 + t_2 + t_3}, \quad (16)$$

$$\tan \theta_v = \frac{h_2}{h_1} \frac{2\sqrt{t_1^2 + t_2^2 + t_3^2 - t_1 t_2 - t_2 t_3 - t_3 t_1}}{t_1 + t_2 + t_3}, \quad (17)$$

$$\cos \varphi_v = \frac{2t_1 - t_2 - t_3}{2\sqrt{t_1^2 + t_2^2 + t_3^2 - t_1 t_2 - t_2 t_3 - t_3 t_1}}, \quad (18)$$

$$\sin \varphi_v = \frac{\sqrt{3}(t_2 - t_3)}{2\sqrt{t_1^2 + t_2^2 + t_3^2 - t_1 t_2 - t_2 t_3 - t_3 t_1}}, \quad (19)$$

When the center probe hits the bubble obliquely at its tip, one or more outer probes should contain invalid signals which should be rejected. Therefore, the minor axis d_{bS} of the bubble is obtained by equation (20), and the sphere equivalent diameter d_{bEq} [m] is obtained by equation (21) by assuming the aspect ratio r_{LS} [-]. The r_{LS} is preset depending on the average diameter of the bubbles.

$$d_{bS} = v_b (t_{ej} - t_{sj}) \Big|_{\max in j=0,1,2,3}. \quad (20)$$

$$d_{bEq} = \sqrt[3]{d_{bL}^2 d_{bS}} = (r_{LS}^{2/3}) d_{bS}. \quad (21)$$

Furthermore, the time-based void fraction α_{F-TOP} [-] is determined from the center probe signal as

$$\alpha_{F-TOP} = C_\alpha \left(\frac{\int_{t=0}^{t_{Total}} V_0 dt}{t_{Total}} - V_{Water} \right) / (V_{Air} - V_{Water}). \quad (22)$$

Considering the geometrical and size relation between an average bubble and the F-TOP, and the deviation of the bubble diameter, the F-TOP can be well tuned so that it

has the best performance to judge whether the pierced position is near the bubble center. If the center probe hits the bubble surface near its tip, one or more outer probes output invalid signals which should be removed. The validation criterion is whether all outer probes output adequate air signals over the threshold th_{Air} during the center probe's transition time from water to air and to water again, or not. Therefore, the minor chord length of the bubble is obtained from equation (20) and the equivalent diameter is obtained from equation (21) by assuming the aspect ratio r_{LS} , which is preset depending on the average diameter of the bubbles.

4.3. Categorization of signal noise in industrial sites

In industrial use of the optical fiber probe, the probe signals include many types of noise. They are grouped into two major categories: electrical noise and optical noise. The electrical noise can be separated into category (A), the power-source noise, and category (B), high-frequency noise.

The noise arises from the transient responses of electrical units and the power supply. The number of electrical noise sources in industrial plants is large; however, they are easily identifiable: electromagnets in heating coils, relay circuits, and motors in fans, pumps, compressors and so on. Most of them are easily removed from the raw signals. By attaching a noise filter component to the power supply of the optical fiber probing electrical units, the category-(A) noise can be removed. By shielding and grounding the power supply unit, the category-(B) noise can be removed.

The optical noise sources are categorized into category (C), oscillation or swing of optical fiber caused by mechanical oscillation or wind, category (D), oscillation of the optical unit of the probe caused by mechanical oscillation, and category (E), electromagnetic waves from fluorescent lights, sunlight and motors.

The noise sources of category (C) are identifiable by the following actions:

- (a) Recording the optical fiber probe signal, with the sensing tip positioned in a steady single phase of air or water,
- (b) Simultaneously measuring and recording the oscillation of bases touching the optical fibers by acceleration sensors, and
- (c) Analyzing the synchronization frequencies of (a) and (b).

The noise sources of category (D) are identifiable by the following actions:

- (e) Mounting a short-size optical fiber probe on the system and recording the signals under the condition of the sensing tip positioned in steady single phase of air or water,
- (f) Simultaneously measuring and recording the oscillation of the optical unit by acceleration sensors, and
- (g) Analyzing the synchronization frequencies of (e) and (f).

The above optical noises are removed easily by the following actions: by covering the optical fiber by pipes and placing them on vibration isolation systems, the noise caused by category (C) and category (E) can be removed. The pipes must be electromagnetic shields. By putting the optical units on vibration isolation systems, the noise caused by category (D) can also be removed. In order to remove the category-(E) noise, the optical unit including photo multipliers and laser diodes should be shielded and isolated electromagnetically.

After removing all the types of noise described above, the optical probing raw signals still include some noisy-like peaks. I investigated the wave patterns carefully and found that they arise from optical phenomena of the sensing tip and air-water interface.

The left of figure 22 shows a raw signal obtained from the probing in an industrial bubble column. It contains spike peaks which force the increase of V_{Max} . The unusual spike peaks disturb the detection of V_{Air} and V_{Water} because the configuration of the threshold parameter ζ is difficult or impossible to discern. Figure 34 shows typical burst

signals extracted from figure 22 after the categorization.

I carefully analyzed the relations between the typical spike peaks and the piercing process of the probe. Figure 35 shows typical snapshots and signal patterns obtained from the experiment of a single bubble hitting an S-TOP.

The following 4 spike peaks were found to arise from the indicated phenomena. The each mechanisms are describing in figures 35 and 36.

Spike peak (1) : reflecting from the frontal surface and focusing from the rear surface of the bubble. I call this a pre-signal. This pattern appears only when the probe pierces the center of a bubble directly.

Spike peak (2) : reflecting from the frontal surface of the bubble. This pattern often appears, and its peak value is uncertain and unpredictable.

Bounding wave (3) : scattering from the oscillating surface.

Spike peak (4) : reflecting and focusing from the rear surface of the bubble. This pattern appears only when a bubble hits the probe obliquely.

These noisy-like peaks are considered as unavoidable physical (optical) phenomena in the optical fiber probing. Therefore, the min-max method shows instability in the signal processing of the first step in figure 21 under industrial measurement conditions.

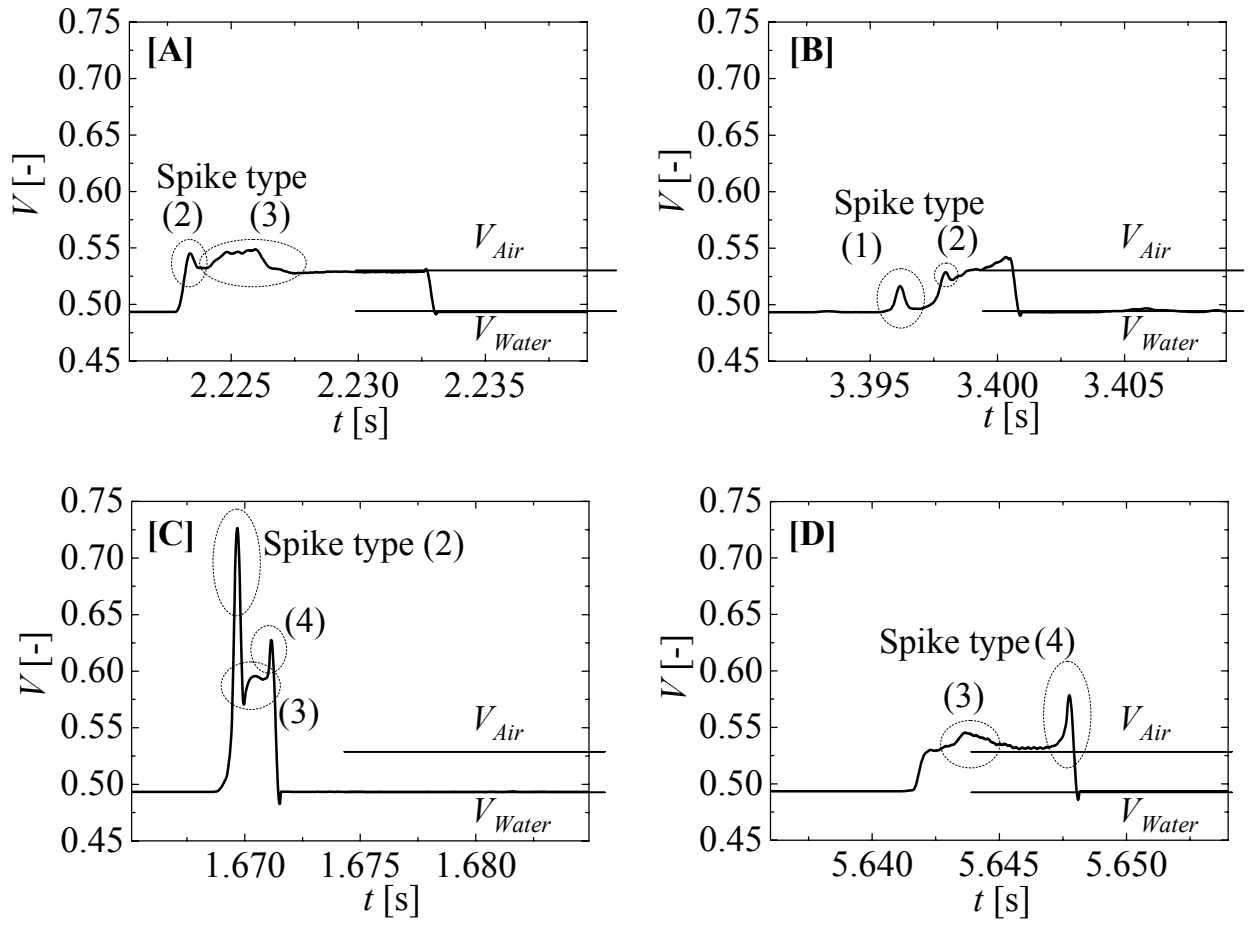


FIG. 34: Noisy burst signal of bubbles.

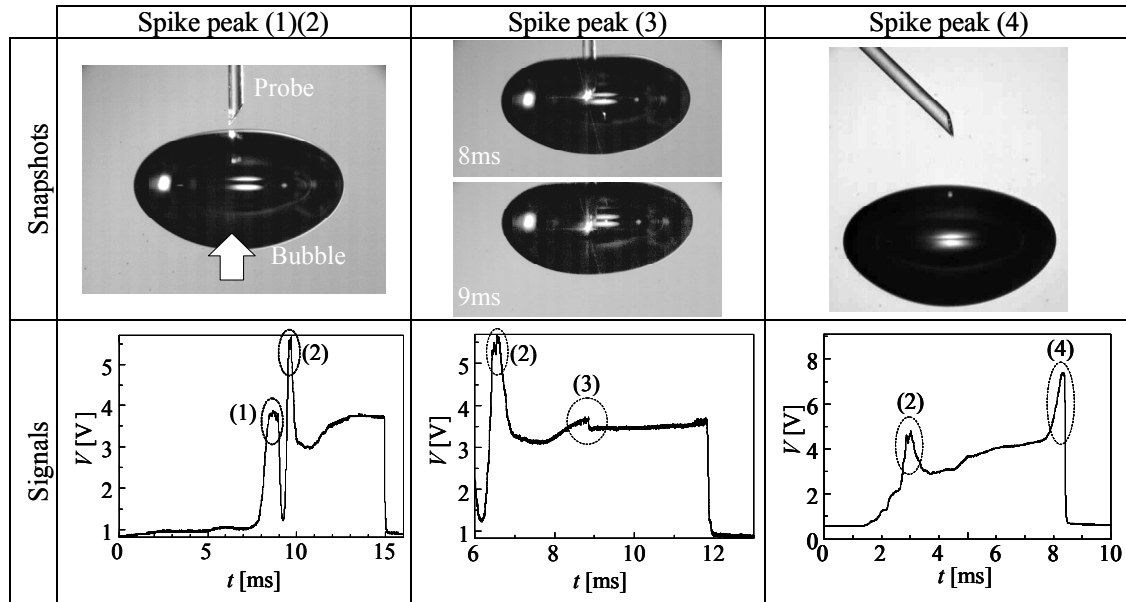


FIG. 35: Snapshots of categorized contact processes and the corresponding signal patterns.

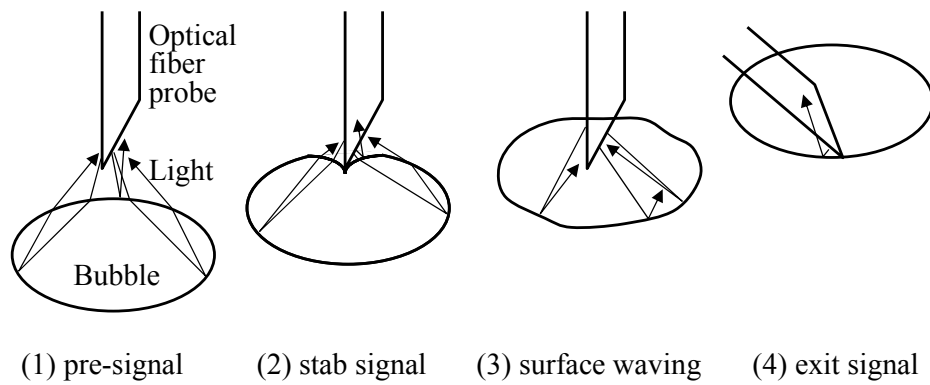


FIG. 36: Mechanisms of the categorized spike peaks based on beam reflection patterns.

4.4. Large-scale bubble column setup

Figures 37 and 38 show a large-scale bubble column to investigate the performance of F-TOP with the new algorithm. 8 needle air injection nozzles of 1.0mm(inner diameters) are set tangentially at the bottom of the column. The bubble diameter ranges from 1 to 4 mm, and the velocity from 0.3 to 0.6 m/s, and the void fraction from 5 to 15%. Bubbles less than 2 mm in equivalent diameter are generated by diluting 1-Octanol by 1.0 ppm-vol⁴⁵. Three F-TOPs were installed in the column. They have optical units including laser diodes and photo diodes, a data recording unit which resolution is 16 bit in 0-5[V], and a signal data processing software implementing the equations (13)-(19) with the histogram method. The signal voltage was normalized from 0-5 [V] to 0-1 [-]. The sampling frequency of the data recorder was 50kHz. In the settings for the F-TOPs and their optics, I made a great effort to remove background noise, as summarized in section 4.3. The results obtained via F-TOP are compared to other measurement techniques. The diameters are compared to those obtained via a visualization method in which the long and short chord lengths of each bubble are measured by pictures captured by still camera, the sphere equivalent diameter is calculated by equation (21), and the distributions and average are analyzed.

The velocities are compared to those obtained via PIV software “Flowvec” developed by Library, Inc. in Japan, which processes video images captured by 30Hz. The void fraction $\alpha_{Manometer}$ [-] is compared to those obtained via a differential pressure method using the following equation;

$$\alpha_{Manometer} = 1 - \frac{\Delta P}{\rho_w g \Delta h} , \quad (23)$$

where ΔP [Pa] is the differential pressure, ρ_w [kg/m³] is water density, g [m/s²] is the gravity and Δh [m] is the vertical length of the measuring section of the ΔP .

Figure 39 shows a micrograph of the F-TOP sensing tip. The gap lengths h_1 and h_2 (see figure 30) were measured from micrographs, as shown in table 4.

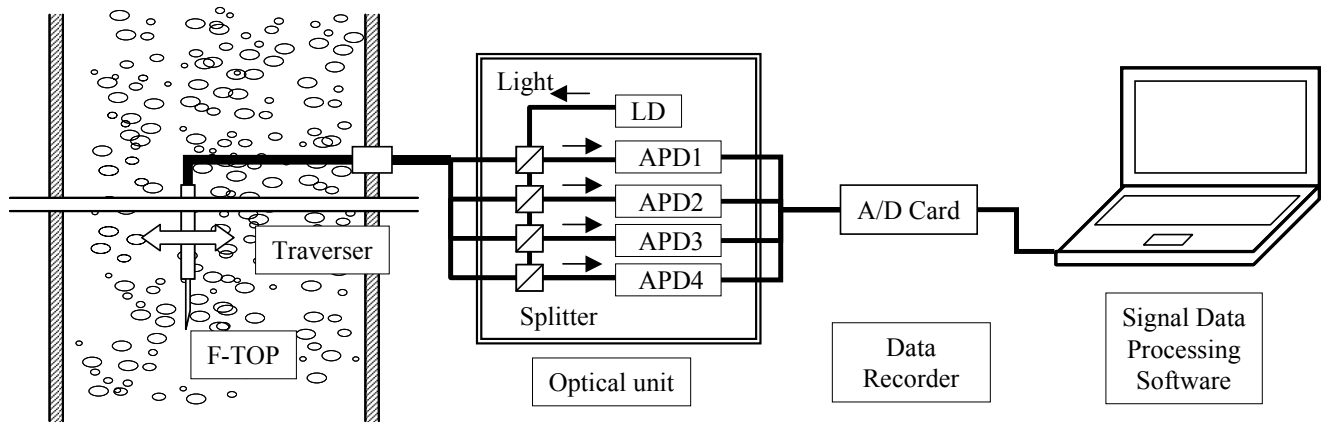


FIG. 38: F-TOP setup.

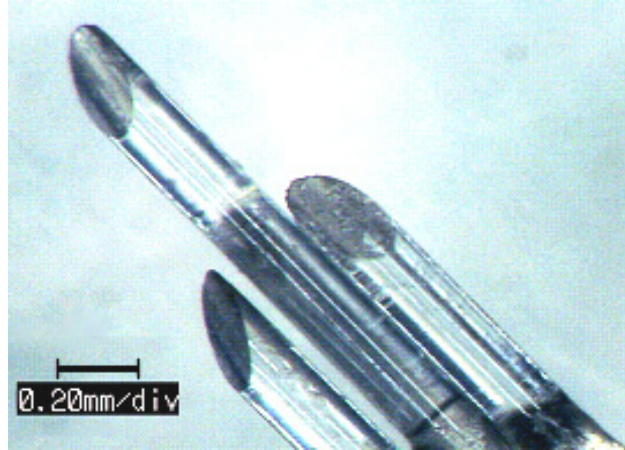


FIG. 39: Micrograph of F-TOP sensing tip.

Table 4: Gap between center and outer probes

	h_1 [μm]	h_2 [μm]
F-TOP6	245.5	972.7
F-TOP7	237.0	905.8
F-TOP8	252.5	1378.0

4.5. Results and discussions

Figures 40-42 show the comparisons of F-TOP measurement and other measurements. Some points of visualization measurements were failed because crowded bubbles caused much misdetection of bubble edges.

Figure 40 shows equivalent diameters of the bubbles measured by F-TOP compared with the visualization results. The plotted symbols represent the averages, and the error bars represent the standard deviations for each measurement. The differences in results via both methods are on average $\pm 15\%$.

Figure 41 shows the velocity of the bubbles measured by the F-TOP compared with the PIV results. The differences in results via both methods are on average $\pm 10\%$.

Figure 42 shows void fractions measured by the F-TOP compared with the results via the differential pressure method. The differences in results are on average $\pm 15\%$. I should pay attention to calibration factor C_α values larger than 1.0 because smaller bubbles are thought to not be detected due to slip at the sensing tip. As a result, the void fraction measured by the F-TOP is less than the volume-based void fraction. It is hypothesized that C_α becomes larger if the bubble diameter is smaller or its velocity is slower, but the relationship is not yet well understood.

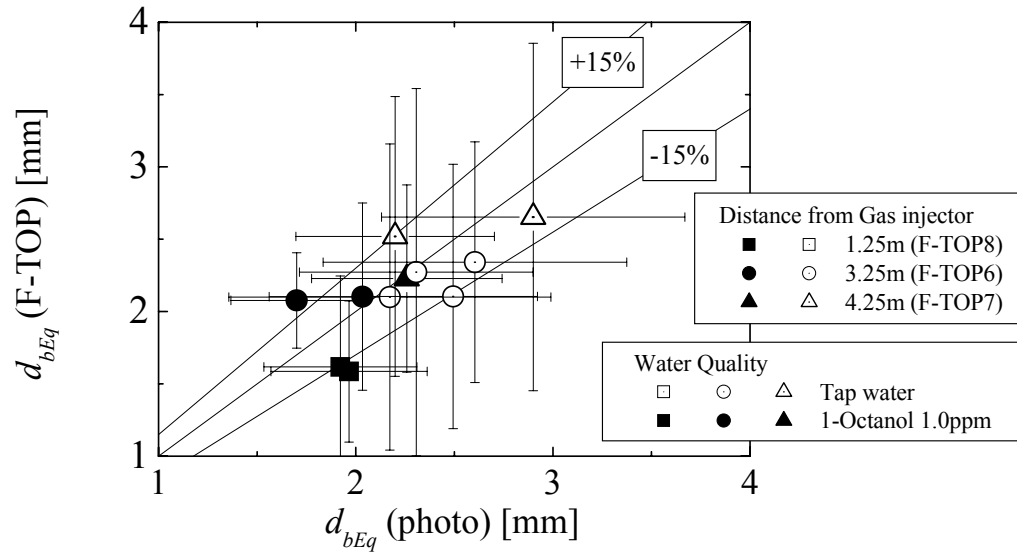


FIG. 40: Measurement result of bubble diameter.

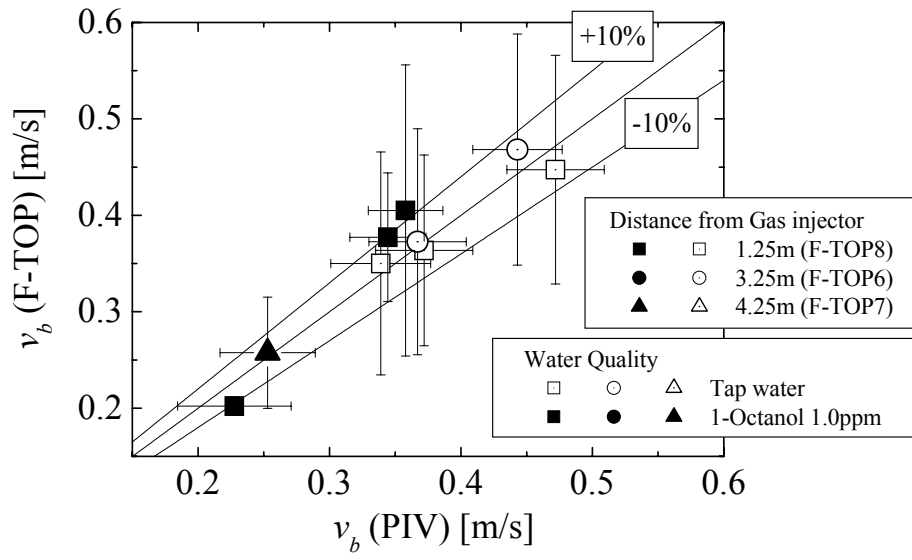


FIG. 41: Measurement result of bubble velocity.

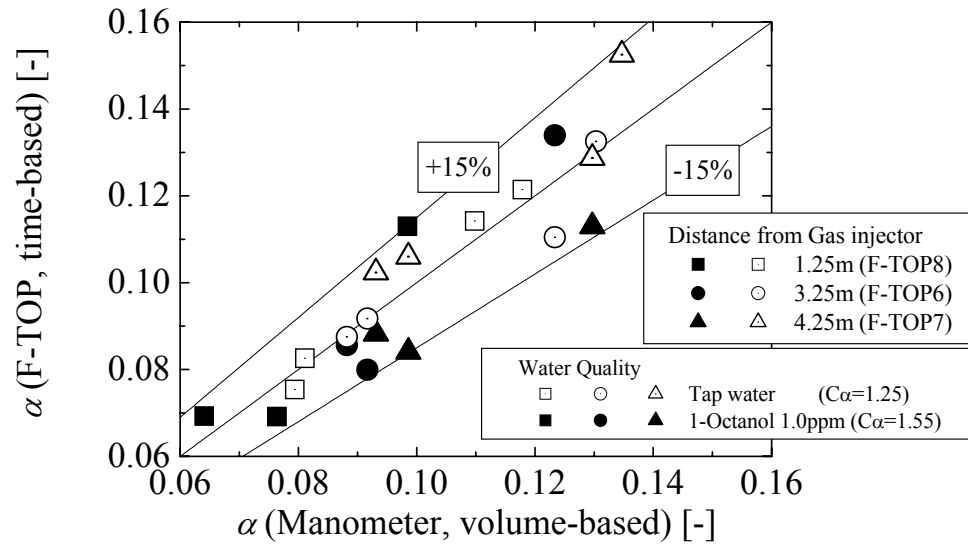


FIG. 42: Measurement result of void fraction.

4.6. Conclusion

I applied the new robust signal-analyzing technique for optical fiber probing in an industrial-scale measurement. Before the measurement, I discussed the sources of electrical and optical noise and techniques to remove them. After removing this noise, the optical fiber probe's signal still includes some peak signals (strong pre-signals and overshoots) that arise from optical phenomena and are inevitable. These peaks depress the stability of the signal processing; I therefore developed more robust algorithms for the histogram and median methods.

I confirm the performance of the optical fiber probing in industrial-scale bubble column (a large-scale bubble column 260 mm in inner diameter and 6 m in height). The bubble diameters ranged from 1 mm to 4 mm; the velocity from 0.2 m/s to 0.6 m/s; and the void fraction from 5 % to 15 %. Comparing other measurement techniques for differential pressure, visualization and PIV, the differences in the average bubble diameters, bubble velocities, and void fractions in the F-TOP measurement were $\pm 15\%$, $\pm 10\%$, and $\pm 15\%$, respectively. This performance is considered to be satisfactory for use in practical industrial measurements.

5. Conclusion

In industrial settings of optical fiber probing, the raw probing signals include a lot of inevitable noise that is very difficult to be eliminated and depresses the measurement accuracy. I categorized the sources of electrical and optical noise and techniques to remove them. After removing the noise, the probing signal still includes some peak signals (strong pre-signals and overshoots) that arise from optical phenomena and are inevitable.

I endeavored to reveal the mechanism of the peak signals by developing a numerical simulator of probing based on ray tracing algorithm. In the simulator, the rays' energy is calculated precisely based on Fresnel's law, furthermore, the whole optical phenomena (i.e., the incident beams, the emitted beams from the sensing tip, the beams reflected and refracted on the air-water interface using polarization angle, the beams re-entered into the sensing tip and beams transmitted through the optical fiber) are calculated in three-dimension. Analyzing probing signals of an S-TOP under some optical conditions computationally, I revealed the following mechanisms:

(1) The optimum angle of the sensing tip for the wedge-shaped S-TOP.

Calculating the emitted-beam trajectories from the sensing tip of the S-TOP, the computational results were well accorded with the experimental results. I obtained the optimum angle range of the wedge-shaped probe from 28° to 32° computationally.

(2) The relation between an interface deformation and the probing signal.

Calculating the signals output from the S-TOP piercing an air-water flat interface, I pointed out the interface deformation obviously affected the probing signals. Under a numerical condition of no deformation of the interface, the calculated signal showed a intensive peak just when the sensing tip touched the interface; this was caused by direct reflection from the interface. Under a numerical condition of a 0.2 mm meniscus radius, the calculated signal was well accorded with the experimental signal.

(3) The mechanism of the pre-signals.

The origins of pre-signals have been identified to the reflected beams from the air-water frontal interfaces in various optical probing studies. I showed it is true in a flat free interface but it is not enough in a bubble. I showed the reflected and focused light from the rear interface of a bubble can be the origin and the peak time changed in association with the curvatures of the bubble rear interface. These phenomena may contribute to advanced bubble/droplet measurement.

After all, the signal processing software of the probing has to have enough robustness even in processing the raw signal including inevitable peak signals. I therefore developed more robust algorithms based on histogram analysis and median analysis. The new algorithms showed a high level of robustness compared with the conventional min-max method in analyzing sample signals obtained from industrial-scale bubble column experiments.

These algorithms were applied to the signals of a four-tip optical-fiber probing employed in industrial-scale measurements of a large-diameter, high-concentration and multi-dispersed bubble column. The bubble column's inner diameter was 260 mm and the height was 6 m. The bubble diameters ranged from 1 mm to 4 mm; the velocity from 0.2 m/s to 0.6 m/s; and the void fraction from 5% to 15%. Comparing other measurement techniques for differential pressure, visualization and PIV, the differences in the average bubble diameters, bubble velocities, and void fractions in the F-TOP measurement were $\pm 15\%$, $\pm 10\%$, and $\pm 15\%$, respectively. This performance is considered to be satisfactory for use in practical industrial measurements.

Nomenclature

E	[C/m ²] Electric field.
B	[Wb/m ²] Magnetic field.
$n, (n_i, n_t)$	[-] refractive index, (of incoming media, of transmitting media.)
c	[m/s] light velocity=2.998×10 ⁸ m/s.
$\varphi()$	[-] Eikonal function.
\mathbf{r}	[m] Ray displacement.
s	[m] Ray displacement between the root point and \mathbf{r} .
θ_i, θ_t	[rad] Incoming angle, transmitting (refracting) angle.
R_p, R_s	[-] Reflectivities of parallel and perpendicular (senkrecht) polarization.
T_p, T_s	[-] Transmissivities of parallel and perpendicular (senkrecht) polarization.
$t_s, (t_{sj})$	[s] Contacting time of bubble (to each probes j.)
$t_e, (t_{ej})$	[s] Leaving time of bubble (from each probes j.) where j=0 means center probe and j=1,2,3 mean outer probes.
V_*	[V] or [-] Voltage measured by photo diode as the probing signal. *=th, Max, Min mean threshold level, the max level, and the minimum level respectively. *=Water, Air, 0 mean water phase level, air phase level, and center probe respectively.
R_1, R_2, R_m, z_m	[m] Meniscus shape parameters (see figure 3.)
R_{Clad}	[m] Radius of clad.
h	[m] Offset of the probe's tip point and flat surface (see figure 3.)
h_f	[m] Cutting length of the probe's sensing tip (see figure 3.)
R_{b1}, R_{b2}	[m] Parts of the minor axis of a bubble (see figure 4.)
θ	[rad] Cutting angle of the probe's sensing tip.
ζ, n, k	[-] Preset parameters of the min-max method, the histogram method and the median method.
ξ_{Water}, ξ_{Air}	[-] Preset threshold parameters.
th_{Water}, th_{Air}	[V] or [-] Threshold levels derived from the equations (12).
\mathbf{v}_b	[m/s] Velocity of a bubble = (v_b, θ_v, φ_v). (see figure 33)
$\mathbf{P}_0, \mathbf{P}_1, \mathbf{P}_2, \mathbf{P}_3$	[m] Coordinates of the center probe tip and outer probe edges.
\mathbf{n}_s	[-] The normal unit vector of the bubble's frontal surface.
t_1, t_2, t_3	[s] = $t_{sj} - t_{s0}$; Time gap of bubble or droplet contacting with each probes j.
h_1	[m] Pitch circle radius of outer probes (see figure30).
h_2	[m] Offset of a center probe and outer probes (see figure30).
d_{bS}, d_{bL}, d_{bEq}	[m] Minor axis, major axis, and sphere equivalent diameter of a bubble.
r_{LS}	[-] = d_{bL} / d_{bS} ; Aspect ratio of bubble or droplet assumed as oblate spheroid.
α	[-] Void fraction.
C_α	[-] Calibration factor of void fraction.
ΔH	[m] Interval of differential pressure detecting points of figure 37.
ΔP	[m] Differential pressure of figure 37.
ρ_w	[kg/m ³] Water density.
g	[m/s ²] Gravity acceleration = 9.80665 m/s ² .

References

1. Abuaf, N., Jones, O. C. Jr. and Zimmer, G. A., 1978. Optical probe for local void fraction and interface velocity measurements, *Review of Scientific instruments*, 49(8), 1090-1094.
2. Albing, C. and Vossen, C., JP, Newham, 2007. *bash Cookbook*, O'Reilly Media.
3. Aprin, L., Mercier, P. and Tadrist, L., 2007. Experimental analysis of local void fractions measurements for boiling hydrocarbons in complex geometry, *International Journal of Multiphase Flow*, 33, 371-393.
4. Bai, W. et al., 2010. Bubble properties of heterogeneous bubbly flows in a square bubble column, *AIP Conference Proceedings*, MF-12.
5. Barrau, E., Riviere, N., Poupot, C. and Cartellier, A., 1999. Single and double optical probes in air-water two-phase flows: real time signal processing and sensor performance, *International Journal of Multiphase Flow*, 25, 229-256.
6. Burgess, J. M. and Calderbank, P. H., 1975. The Measurement of Bubble Parameters in Two-Phase Dispersions-I, *Chemical Engineering Science*, 30, 743-750.
7. Burgess, J. M. and Calderbank, P. H., 1975. The Measurement of Bubble Parameters in Two-Phase Dispersions-II, *Chemical Engineering Science*, 30, 1107-1121.
8. Burgess, J. M. and Calderbank, P. H., 1975. The Measurement of Bubble Parameters in Two-Phase Dispersions-III, *Chemical Engineering Science*, 30, 1511-1518.
9. Cartellier, A. and Achard, J.L., 1991. Local phase detection probes in fluid/fluid two-phase flows, *Review of Scientific Instruments*, 62, 279-303.
10. Cartellier, A. and Barrau, E., 1998. Monofiber optical probes for gas detection and gas velocity measurements: conical probes, *International Journal of Multiphase Flow*, 24, 1265-1294.
11. Cartellier, A. and Barrau, E., 1998. Monofiber optical probes for gas detection and gas velocity measurements: optimised sensing tips, *International Journal of Multiphase Flow*, 24, 1295-1315.
12. Cartellier, A., 1998. Measurement of gas phase characteristics using new monofiber optical probes and real-time signal processing, *Nuclear Engineering and Design*, 184, 393-408.
13. Chaumat, H. et al., 2007. Hydrodynamics and mass transfer in bubble column: Influence of liquid phase surface tension, *Chemical Engineering Science*, 62, 7378-7390.

14. Clanet, C., and Quere, D., 2002. Onset of menisci, *J. Fluid Mech.*, 460, 131-149.
15. Dunn, F. and Parberry, I., 2011. 3D Math Primer for Graphics and Game Development, 2nd Edition, CRC Press.
16. Fan, L.-S. and Tsuchiya, K., 1990. Bubble Wake Dynamics in Liquids and Liquid-Solid Suspensions, Butterworth-Heinemann Series in Chemical Engineering.
17. Frijlink, J. J., 1987. Physical aspects of gassed suspension reactors, PhD thesis, TU Delft.
18. Harteveld, 2005. Bubble columns - structure or stability?, PhD thesis, TU Delft.
19. Higuchi, M., Saito, T., 2010. Quantitative characterizations of long-period fluctuations in a large-diameter bubble column based on point-wise void fraction measurements, *Chemical Engineering Journal*, 160, 284-292.
20. Hong, M., Cartellier, A. and Hopfinger, E. J., 2004. Characterization of phase detection optical probes for the measurement of the dispersed phase parameters in sprays, *International Journal of Multiphase Flow*, 30, 615-648.
21. Julia, J.-E., 2005. On the accuracy of the void fraction measurements using optical probes in bubbly flows, *Review of Scientific Instruments*, 76, 35103.
22. Kernighan, B. W. and Ritchie, D. M., 1972. *The C Programming Language*, Prentice Hall.
23. Kiambi, S. L. et al., 2003. Measurements of Bubble Characteristics, Comparison Between Double Optical Probe and Imaging, *The Canadian Journal of Chemical Engineering*, 81, 764-770.
24. Kitware, 2010. *The VTK User's Guide 11th edition*, Kitware.
25. Mahvash, A., and Ross, A., 2008. Two-phase flow pattern identification using continuous hidden Markov model, *International Journal of Multiphase Flow*, 34, 303-311.
26. Mena, P. C., Rocha, F. A., Teixeira, J. A., Sechet, P. and Cartellier, A., 2008. Measurement of gas phase characteristics using a monofibre optical probe in a three-phase flow, *Chemical Engineering Science*, 63, 4100-4115.
27. Mizuno, Y. and Saito, T., 2005. Formulation of four-tip optical-fiber probe for accurate characterization of bubbles, *IASME Transactions*, 2(9), 1612-1618.
28. Moore, D. T., 1975. Ray tracing in gradient-index media, *Journal of the Optical Society of America*, 65, 451-455.
29. Mudde, R. F. and Saito, T., 2001. Hydrodynamical similarities between bubble column and bubbly pipe flow, *Journal of Fluid Mechanics*, 437, 203-228.
30. Nakamura, H., Saiki, T., Kambe, H., Sawada, K., 2001. FDTD simulation of tapered structure of near-field fiber probe, *Computer Physics Communications*, 142,

464-467.

31. Nakamura, H., Sato, T., Kambe, H., Sawada, K. and Saiki, T., 2001. Design and optimization of tapered structure of near-field fibre probe based on finite-difference time-domain simulation, *Journal of Microscopy*, 202, Pt 1, 50-52.
32. Nicodemus, F.E., Richmond, J.C., Hsia, J.J., Ginsberg, I.W. and Limperis, T., 1977. Geometrical Considerations and Nomenclature for Reflectance, NBS Monograph, 160.
33. Riviere, N., et. al., 1999. Wall shear stress and void fraction in Poiseuille bubbly flows, *Eur. J. Mech. B, Fluids* 18, 847-867.
34. Saito T., et al, 2004. Research about Optical Fiber Sensor Contributing Energy Saving Processes to separate and stock CO₂, *Proceeding of Meeting in Italic*, 2003rd R&D consortium project of economic stimulus for the region, METI-Kanto, 15G3042.
35. Saito, T. and Mudde, R. F., 2001. Performance of 4-tip Optical Fiber Probe and Bubble Characterizations by the Probe in Turbulent Bubbly Flows, *Proc. of International Conference for Multi-phase Flow*, No.111, in CD-ROM.
36. Saito, T., 2000. Method and Apparatus for Bubble Measurement using Optical Fiber, Japanese Patent No. 3018178.
37. Saito, T., Matsuda, K., Ozawa, Y, Oishi S. and Aoshima, S., 2009. Measurement of tiny droplets using a newly developed optical fiber probe micro-fabricated by a femtosecond pulse laser, *Measurement Science and Technology*, 20, 114002.
38. Saito, T., Sakakibara, K., Miyamoto, Y. and Yamada, M., 2010. A Study of Surfactant Effects on the Liquid-Phase Motion around a Zigzagging-ascent Bubble Using a Recursive Cross Correlation PIV, *Chemical Engineering Journal*, Elsevier, 158, 39–50.
39. Sakamoto, A. and Saito, T., 2010. Numerical Analysis of Optical Fiber Probing by Ray Tracing Method, *15th International Symposium on Applications of Laser Techniques to Fluid Mechanics*, 1643.
40. Sakamoto, A. and Saito, T., 2012. Robust algorithms for quantifying noisy signals of optical fiber probes employed in industrial-scale practical bubbly flows, *International Journal of Multiphase Flow*, 41, 77–90.
41. Sakamoto, A. and Saito, T., 2012. Computational analysis of responses of a wedge-shaped-tip optical fiber probe in bubble measurement, *Review of Scientific Instruments*, 83, 7, 075107.
42. Schlick, C., 1994. An Inexpensive BRDF Model for Physically-based Rendering, *Computer Graphics Forum*, 13, 3, 233-246.
43. Shirota, M., Sanada, T., Sato, A. and Watanabe, M., 2008. Formation of a

- submillimeter bubble from an orifice using pulsed acoustic pressure waves in gas phase, *Physics of Fluids* 20, 043301.
44. Sweat, W. C., 1977. Describing holographic optical elements as lenses, *Journal of the Optical Society of America*, 67, 803.
 45. Takagi, S., 2004. The Effect of Surfactant on the Motion of Rising Bubbles, *Nagare*, 23, 17-26.
 46. Vejrazka, J., Vecer, M., Orvalho, S., Sechet, P., Ruzicka, M. C. and Cartellier, A., 2010. Measurement accuracy of a mono-fiber optical probe in a bubbly flow, *International Journal of Multiphase Flow*, 36, 533-548.
 47. Wedin, R., Davoust, L., Cartellier, A. and Byrne, P., 2003. Experiments and modeling on electrochemically generated bubbly flows, *Experimental Thermal and Fluid Science*, 27, 685-696.
 48. Xue, J., 2004, Bubble Velocity, Size and Interfacial Area Measurements in Bubble Columns, PhD thesis, Washington University.